Single-cell dissection of prognostic architecture and immunotherapy response in *Helicobacter pylori* infection associated gastric cancer

Running title: Single-cell transcriptomic architecture of *H. pylori*$^{+}$ GC

Authors: Xin Zhang[1,2,#], Guangyu Zhang[4,#], Shuli Sang[1,#], Yang Fei[5,#], Xiaopeng Cao[6,#], Wenge Song[1], Feide Liu[5], Jinze Che[5], Haoxia Tao[1], Hongwei Wang[7], Lihua Zhang[7], Yiyan Guan[1], Shipeng Rong[5], Lijuan Pei[5], Sheng Yao[5,*], Yanchun Wang[1,*], Min Zhang[3,*], Chunjie Liu[1,*]

Affiliations:

1 State Key Laboratory of Pathogen and Biosecurity, Institute of Biotechnology, Academy of Military Medical Sciences, Beijing, China.

2 Department of Pharmacy, Medical Supplies Center, Chinese PLA General Hospital, Beijing, China.

3 Department of Nephrology, First Medical Center of Chinese PLA General Hospital, Beijing, China.

4 Guangzhou Institutes of Biomedicine and Health, Chinese Academy of Sciences, Guangzhou, China.

5 Department of General Surgery, First Medical Center, Chinese PLA General Hospital, Beijing, China.

6 Department of Gastroenterology and Hepatology, First Medical Center, Chinese PLA general hospital, Beijing, China.

7 Department of Pathology, Fourth Medical Center, Chinese PLA General Hospital, Beijing, China.

Correspondence:

Prof Chunjie Liu and Prof Yanchun Wang, State Key Laboratory of Pathogen and Biosecurity, Institute of Biotechnology, Academy of Military Medical Sciences, Beijing, 100071, China; liucj@bmi.ac.cn, springwyc@163.com

Dr Min Zhang, Department of Nephrology, First Medical Center of Chinese PLA General Hospital, Beijing, 100853, China; mzhangcool@163.com

MD Sheng Yao, Department of General Surgery, First Medical Center of Chinese PLA General Hospital, Beijing, 100853, China; ys848388@163.com

# These authors contributed equally

ABSTRACT

Most of the gastric cancer (GC) worldwide are ascribed to *Helicobacter pylori* (*H. pylori*) infections, which have a detrimental effect on the immunotherapy's efficacy. Comprehensively dissecting the key cell players and molecular pathways associated with cancer immunotherapies is critical for developing novel therapeutic strategies against *H. pylori* infection associated GC. We performed a comprehensive single-cell transcriptome analysis of nine GC with current *H. pylori* infection (HpGC), three GC with previous *H. pylori* infection (ex-HpGC), six GC without *H. pylori* infection (non-HpGC), and six healthy controls (HC). We also investigated key cell players and molecular pathways associated with GC immunotherapy outcomes. We revealed the molecular heterogeneity of different cell components in GC including epithelium, immune cells, and cancer-associated fibroblasts (CAFs) at the single-cell level. The malignant epithelium of HpGC exhibited high expression level of inflammatory and epithelial-mesenchymal transition (EMT) signature, HpGC and ex-HpGC were enriched with VEGFA+ angiogenic tumor-associated macrophages (Angio-TAM) and IL11+ inflammatory CAF (iCAF), characterized by high expression levels of NECTIN2 and VEGFA/B. Additionally, we found significant correlations between the abundance of iCAF with Angio-TAM and TIGIT+ suppressive T cells, and iCAF interacted with Angio-TAM through the VEGF and ANGPTL angiogenic pathways. We also developed an immune signature and angiogenic signature and demonstrated that the iCAF abundance and angiogenic signature could predict poor immunotherapy outcomes in GC.We revealed the transcriptome characteristics and heterogeneity of various cellular constituents of HpGC and demonstrated that a synergistic combination of immunotherapy and anti-angiogenic targeted therapy may be an effective therapeutic modality for HpGC.

Keywords: Single-cell sequencing; *Helicobacter pylori* infection; Inflammatory cancer-associated fibroblast; Immunotherapy; Anti-angiogenic targeted therapy

Introduction

Gastric cancer (GC) is the fifth most diagnosed tumor and the third most common cause of cancer-causing death. GC is characterized by heterogeneous cellular characteristics and a tumor microenvironment (TME) comprising complex components, posing challenges to personalized therapy (*1*). The development of GC can be attributed to the long-term combined effects of lifestyle, environmental factors, genetic factors, and pathogenic infections.

Helicobacter pylori (*H. pylori*) infection (*2, 3*) is an important carcinogenic factor, and responsible for approximately 90% of noncardia GC worldwide and approximately 5% of the total burden from all cancers globally (*4*). It also plays a critical role in TME regulation and is linked to response to immunotherapies (*5, 6*). According to the histological examination, serology test, rapid urease test, and *H. pylori* DNA validation, *H. pylori* infection associated GC cases can be classified to current *H. pylori* infection and past *H. pylori* infection, and the *H. pylori* infection status correlated with different molecular characteristics (*7, 8*).

Immune checkpoint inhibitor (ICI)-targeted therapy is an effective anti-cancer treatment for a wide range of human malignancies (*9-12*). However, their efficacy in GC remains controversial (*13*). Previous clinical trial studies such as JAVELIN Gastric 300 (*14*), KEYNOTE-061 (*15*), and KEYNOTE-062 (*16*) have shown that PD-1/PD-L1 inhibitors do not have significant advantages over conventional chemotherapy in the treatment of GC. In contrast, the CheckMate-649 study has revealed that the continued use of nivolumab plus chemotherapy as a standard first-line treatment achieved great success in advanced gastroesophageal adenocarcinoma (*17*). A subgroup analysis has revealed that the Asian population benefits more from immunotherapy than the global population, and among the Asian population, the Chinese population benefits the most from immunotherapy, which could be ascribed to the molecular features leading to GC in Chinese patients, such as *H. pylori* infection (*18, 19*). However, recent studies have demonstrated that *H. pylori* infection hindered the efficacy of immune checkpoint-targeting PD-1/PD-L1 inhibitors or vaccine-based immunotherapies through immune evasion, T cell suppression, and fluctuation in the intestinal flora, compromising the benefits of cancer immunotherapies (*5, 13*). The cellular and molecular heterogeneity of *H. pylori* infection associated GC prevent effective immunotherapies; thus, revealing the discrepancy in the molecular characteristics of various cellular components among GC patients with different *H. pylori* infection status is required for accurate diagnosis and treatment.

The continued availability of single-cell RNA sequencing (scRNA-seq) has allowed systematic profiling of dynamic transcriptional characteristics of thousands of cells simultaneously at the single-cell level with high throughput and low cost, enabling unbiased deciphering of the molecular heterogeneity of various components in biological tissues (*20, 21*) . A previous study has applied scRNA-seq technology in various types of gastric mucosa biopsies with different lesions to reveal dynamic transcriptional changes in the cascade of GC and to construct a transcriptional regulatory network in the gastric epithelium (*22*). We have also previously constructed a systematic transcriptomic landscape of gastric adenocarcinoma and profiled the developmental trajectory of GC (*23*). Additionally, scRNA-seq has been used to dissect TME heterogeneity (*24*) and molecular features of various

88 components in the GC TME, including immune cell diversity, which facilitates the understanding of tumor biology
89 and sheds light on novel targets for immunotherapy (*25-27*). However, little attention has been paid to the
90 relationship between *H. pylori* infection, diversity of GC TME, and immunotherapy response at the single-cell
91 level.

92 This study aimed to reveal the diversity of the *H. pylori* infection associated GC TME and to distinguish key
93 cellular players, molecular pathways, and effector programs associated with response to immunotherapies in GC.
94 We performed unbiased scRNA-seq on gastric tissues of healthy control (HC, n=6), GC without *H. pylori* infection
95 (non-HpGC, n=6), GC with current *H. pylori* infection (HpGC, n=9), and GC with previous *H. pylori* infection
96 (ex-HpGC, n=6) to present the first cellular atlas including a total of 83,637 high-quality cells for deciphering *H.*
97 *pylori* infection associated transcriptomic architecture. We also profiled the intercellular crosstalk among
98 suppressive T cells, angiogenic tumor-associated macrophages (Angio-TAMs), and inflammatory cancer-
99 associated fibroblasts (iCAFs), which correlated with prognosis and response to immunotherapy. In particular,
100 iCAFs that were linked to Angio-TAM and suppressive T cells exhibited upregulation of NECTIN2 and VEGFA/B
101 (vascular endothelial growth factor A/B), which is indicative of poor immunotherapy efficacy. Moreover,
102 intercellular crosstalk analysis revealed that iCAFs may promote tumor angiogenesis and immune suppression in
103 *H. pylori* infection associated GC, by intercellular interaction with Angio-TAM through the VEGFA/B-VEGFR1
104 pathway, and TIGIT^{+} suppressive T cells through the NECTIN2-TIGIT pathway, respectively. Our study indicates
105 that the combination of immunotherapy and vascular-targeted therapies could be a potentially efficient approach
106 for the treatment of *H. pylori* infection associated GC patients.
107

108 **Results**

109 **Single-cell transcriptomic architecture and molecular features of *H. pylori* infection associated GC**

110 In this study, we first classified the collected GC tissues into non-HpGC, HpGC, and ex-HpGC to accurately
111 evaluate the *H. pylori* infection status of GC patients, which was defined by a combination of serology
112 examinations along with the *H. pylori* DNA assay and histological examination (HE) of each gastric tissue
113 (methods, table 1). The gastric tissues selected were collected from six healthy donors (HC) and six non-HpGC,
114 nine HpGC, and six ex-HpGC patients, who were recently diagnosed and did not receive chemotherapy and
115 radiotherapy before surgery (Fig. 1A). Viable cells with high quality were collected from each gastric tissues for
116 further scRNA-seq using fluorescence-activated cell sorting (FACS). A total of 83,637 cells were retained for

subsequent analysis after rigorous quality control, which yielded an average of 1,358 genes and 3,465 transcripts in each cell (fig. S1, A to D). We first employed the inferCNV to evaluate copy number variation (CNV) of autosomal genes among all cells to distinguish malignant and non-malignant cells (fig. S1E), We then identified and annotated nine main cell types according to the expression of canonical gene markers and CNV distribution, which were composed of the non-malignant epithelium (marked with *MUC5AC*, *GKN1*, and *TFF1/2*), malignant epithelium (*KRT17*, *S100A9* and *REG4*), endothelium (marked with *PECAM1*,*VWF* and *PLVAP*), fibroblasts (marked with *DCN*, *LUM* and *COL1A1*), plasma cells (marked with *JCHAIN* and *CD49A*), monocyte/macrophage (marked with *C1QA/B/C* and *IL1B*), mast cells (marked with *CPA3* and *TPSAB1*), B cells (marked with *CD79A* and *MS4A1*), and T cells (marked with *CD2*, *CD3D*, and *CD3E*) (Fig. 1, B to E, fig. S1F, and table S1). To investigate the influence of *H. pylori* infection on the heterogeneity of gastric TME, we analyzed the dynamic cellular component changes of gastric TME in non-HpGC, ex-HpGC and HpGC compared with that of HC. The results revealed a significant increase in the proportion of T cells in GC including non-HpGC, ex-HpGC and HpGC in contrast with HC (Fig. 1, F and G and fig. S2A), which aligned with consensus that tumorigenesis is accompanied by inflammation. In addition, the percentage of non-malignant epithelium significantly decreased in GC compared to normal HC. Whereas, there was a significant increase in the proportion of malignant epithelium in GC compared with that of HC, which is closely related to the process of carcinogenesis. However, there is no significant difference in the proportion of non-malignant epithelium and malignant epithelium among the non-HpGC, ex-HpGC and HpGC (Fig. 1G). To further elucidate the correlation between *H. pylori* infection and the transformation of non-malignant epithelium into malignant epithelium during gastric carcinogenesis, we performed comparative analysis of upregulated genes characteristics between non-malignant epithelial cells and malignant epithelial cells. The result revealed that upregulated genes in the non-malignant epithelium included *MUC5AC*, *GKN1*, and *TFF2*, which participate in secretion of stomach mucus and digestive enzymes, whereas upregulated genes in the malignant epithelium included *TM4SF1*, *IFITM3*, *IGFBP7* and *KRT17* (Fig. 1H and fig. S1, F and G). Gene set enrichment analysis (GSEA) showed that the differentially upregulated genes in the malignant epithelium compared to non-malignant epithelium were enriched in pathways associated with tumor development and progression such as hypoxia, tumor invasiveness, MYC targets, and epithelial-mesenchymal transition (EMT) (Fig. 1I). In brief, our results provided a comprehensive landscape of the cellular and transcriptomic diversity within the cell components in gastric TME associated *H. pylori* infection.

146 **Cellular characterization of the malignant epithelium of *H. pylori* infection associated GC**

147 To further explore the molecular features of *H. pylori* infection associated GC and the heterogeneity of the
148 malignant epithelium, we performed a sub-clustering analysis of malignant cells and generated six distinct
149 malignant epithelium subpopulations (M1–M6), in which clusters M1 and M2 were mainly derived from non-
150 HpGC, whereas clusters M5 and M6 were mainly originated from *H. pylori* infection associated GC samples
151 including HpGC and ex-HpGC (Fig. 2, A and B and fig. S2, A and B). The expression distribution of these clusters
152 was validated in HpGC by deconvolution analysis using bulk RNA sequencing datasets (Wilcoxon test; fig. S2C)
153 (*28*). We found that malignant epithelium of M1/M2/M3/M4 exhibited high expression levels of epithelium
154 differentiation-related genes, such as *PHGR1* and *KRT20* (Fig. 2C), whereas M5/M6 or *H. pylori* infection
155 associated GC samples exhibited high expression levels of inflammation-related genes, such as *CXCL1/2/3/8*,
156 *S100A9*, *S100P*, and EMT signature, such as *SPARC* and *VIM* (Fig. 2, C and D). In addition, among the *H. pylori*
157 infection associated GC samples, the expression of inflammation-related genes and IgG family members' genes
158 were much higher in HpGC (Fig. 2D, fig. S2D and table S2). Interestingly, GSEA of the upregulated genes in the
159 HpGC malignant epithelium were mainly associated with EMT, epithelial cell proliferation, and inflammatory
160 response pathways (Fig. 2E). We also found that the malignant epithelium exhibited a high degree of
161 differentiation inter- and intra-heterogeneity (Fig. 2, F and G), the differentiation score of ex-HpGC2 and ex-
162 HpGC5 presented two distinct peaks, one of which is comparable to the peak observed in HpGC, while the another
163 of which resembled the peak observed in non-HpGC sample (Fig. 2F). The finding suggested that a history of *H.*
164 *pylori* infection in GC can still contribute to the differentiation heterogeneity of malignant epithelium.
165 Furthermore, malignant epithelium from ex-HpGC displayed low differentiation scores, which were even lower in
166 malignant epithelium of HpGC ($P < 0.05$, Wilcoxon test; Fig. 2H). This further substantiate the correlation
167 between the inflammatory and differentiation ability with the severity of *H. pylori* infection. Furthermore, the
168 abundance of malignant epithelium cluster could predict different prognosis outcomes (fig. S2E), and the high
169 differentiation score is highly associated with a better prognosis of GC and vice versa (Fig. 2I).

170 Collectively, the findings highlight the transcriptomic heterogeneity of malignant epithelium with different *H.*
171 *pylori* infection status and the potential utility of the molecular features within the malignant epithelium to
172 distinguish HpGC from non-HpGC, indicative of a high degree of tumor heterogeneity and the influence of the *H.*
173 *pylori* infection on gastric carcinogenesis and prognosis.

174

175 **Cellular characterization of the non-malignant epithelium of *H. pylori* infection associated GC**

176 To determine the cellular phenotype and composition of the gastric mucosa during the progression of *H. pylori*
177 infection, we performed a transcriptomic analysis of the non-malignant epithelium, and these cells were partitioned
178 into nine cell types (Fig. 3A), including chief cells (marked by *PGA3*, and *PGA4*), neck cells (marked by *MUC6*),
179 spasmolytic polypeptide-expressing metaplasia (SPEM, marked by *MUC6* and *TFF2*), intestinal metaplasia (IM,
180 marked by *MUC2*), enterocytes (marked by *APOC3* and *FABP1*), endocrine cells (marked by *CHGA*), pit mucous
181 cell (PMC, marked by *GKN1/2* and *MUC5AC*), pre-PMC (marked by medium expression level of *MUC5AC* and
182 *GKN2*), and parietal cells (marked by *ATP4A*) (Fig. 3, B and C, and table S3). We compared the composition of
183 cells in normal mucosae with that of GC mucosae and observed that the neck cell (P = 0.034, Student's t-test),
184 chief cell (P = 0.014, Student's t-test) and parietal cells (P =0.0087, Student's t-test) decreased dramatically in
185 HpGC compared to HC, whereas the HpGC exhibited increase partition of metaplasia lineage SPEM (P = 0.017,
186 Student's t-test) and intestinal-specific cell types, such as IM (P = 0.036, Student's t-test) and enterocytes (P =
187 0.036, Student's t-test). Furthermore, HpGC samples had even a higher proportion of metaplasia lineage SPEM and
188 intestinal-specific cell types and a lower proportion of neck cells and parietal cells than that of ex-HpGC and non-
189 HpGC (Fig. 3C). To conform the validity of our findings, we performed deconvolution analysis with independent
190 microarray data (GSE2669) including 124 normal mucosa control (NC), chronic gastritis (CG), intestinal
191 metaplasia (IM), GC associated with *H. pylori* infection samples to decipher the changes in the proportion of cell
192 components with different stages of gastric tissue. Consistent with our scRNA-seq findings, the proportion of
193 SPEM, IM and enterocytes in GC increased gradually during the gastric carcinogenesis process, with even higher
194 proportion in GC compared with that of CG and IM. In contrast, the proportion of chief cells, neck cells and
195 parietal cells decreased significantly in GC, with the lowest proportion in GC compared with that of CG and IM (P
196 < 0.05, Student's t-test; Fig. 3, D and E). These findings further support the validity of our results and indicates that
197 chronic atrophic gastritis induced by *H. pylori* infection is the main cause of premalignant lesions.

198 To explore the origin of the premalignant cellular lineage and possible transition mechanism, we performed a
199 single-cell analysis to reveal the developmental trajectories of various cell types in the non-malignant epithelium
200 of GC (Fig. 3F). The results showed that chief cells would differentiate into necks, and then the developmental
201 path would divide these cells into two branches, one of which would develop into SPEM, whereas the other
202 represents SPEM that could further develop into IM and enterocytes through transition states under a persistent
203 inflammatory stimulus (Fig. 3G). In addition, the pattern of pseudotemporal dynamic expression of specific

representative genes and transcription factors (TFs) also supports the transition of chief cells to SPEM and IM metaplasia status and finally enterocytes (Fig. 3, H and I).

In brief, our results reveal the transition of GC non-malignant epithelium from chief cells to neck cells, SPEM and IM, and finally to enterocytes, under chronic inflammation at the single-cell level, which may deepen our understanding of the role of *H. pylori* infection in GC.

Cellular characterization of T lymphoid cells of *H. pylori* infection associated GC

Tumor infiltrating lymphocytes (TILs) are highly heterogeneous lymphocyte subsets. The activation of the different subsets of effector T cells influences the clinical outcome of *H. pylori* infection. Sub-clustering of T lymphoid cells and natural killer (NK) cells generated 11 main cell clusters in HC, non-HpGC, ex-HpGC and HpGC (Fig. 4A), including innate lymphoid cell (ILC, marked by *KIT*, *LST1*, and *ZBTB16*), NK1 (marked by *TYROBP*, *GZMA*, and *CEBPD*), NK2 (marked by *NKG7*, *CCL3*, *GZMH*, and *EOMES*), Treg (marked by *FOXP3*, *BATF*, and *TIGIT*), proliferative CD8_MKI67 (marked by *MK167*, and *CXCL13*), exhausted CD8_CXCL13 (marked by *CXCL13* and *TIGIT*), CD8_GZMK (marked by *GZMK*, *CCL4*, and *YBX3*), effective CD8_IFNG (marked by *IFNG*, *ATF3*), cytotoxic CD8_GZMB (marked by *GZMB*, *KLRC1*, and *MYBL1*), naïve CD4_IL7R (marked by *CCR7*, *SELL*, and *CD40LG*) and CD4_CCR7 (marked by *CCR7*, *SELL*, and *CD40LG*) (Fig. 4, B and C, and table S4). The organization of the T cell compartment showed great differences in GC with different *H. pylori* infection status (Fig. 4D). The exhausted CD8_CXCL13, CD8_MKI67 and Tregs were prominently enriched in ex-HpGC and HpGC samples compared to that in HC ($P < 0.05$, Student's t-test; Fig. 4E), with a higher percentage in ex-HpGC and HpGC than in non-HpGC. The cytotoxic CD8_GZMB level was significantly decreased in ex-HpGC and HpGC ($P < 0.05$, Student's t-test; Fig. 4E), which coincides with previous research indicating immunosuppression in the TME. The deconvolution analysis using The Cancer Genome Atlas (TCGA) GC bulk dataset (*29*) indicated that the abundance of Treg and CD8_CXCL13 were elevated in HpGC than non-HpGC ($P = 0.018$, and $= 0.12$, respectively, Wilcoxon test; Fig. 4F). Next, we calculated the cytotoxic and inhibitory scores across various T lymphoid cell types, revealing that two subtypes of NK cells have the highest cytotoxic score, indicative of apoptosis, and Tregs have the highest inhibitory score, implying immunosuppression (Fig. 4G). Overall survival analysis demonstrated that a high proportion of Tregs and CD8_CXCL13 represent a worse prognosis ($P = 0.022$ and $= 0.22$, respectively, log-rank test; Fig. 4H). TIGIT, an important immune checkpoint with ligands including PVR and NECTIN2, is highly expressed in various immune cell types, particularly in Tregs within the TME, and is emerging as an immunotherapy target (*30-32*). Interestingly, we also

found that the suppressive T cells, including Treg and CD8_CXCL13, interacted closely with the malignant epithelium through TIGIT-PVR/NECTIN2 ligand-receptor pairs, with even stronger interactions between suppressive T cells and malignant epithelium M4 and M6 (Fig. 4I). Interestingly, NECTIN2 and PVR were more enriched in ex-HpGC and HpGC, compared with non-HpGC (Fig. 4J). Immunostaining of HpGC also revealed that suppressive TIGIT^{+} T cells were located close to the pan-CK^{+} NECTIN2^{+} malignant epithelium (Fig. 4K), which supported the transcriptional findings that suppressive T cells could interact with the malignant epithelium through TIGIT–NECTIN2/PVR pairs. Collectively, we found that HpGC and ex-HpGC exhibits high expression levels of NECTIN2, PVR, and its target TIGIT, which may participate in immune escape in GC, indicated that blockade of TIGIT-NECTIN or TIGIT-PVR axes may be a promising immunotherapy modality for *H. pylori* infection associated GC.

Cellular characterization of myeloid cells of *H. pylori* infection associated GC

Myeloid cells are also an important component of tumor-infiltrating immune cells, which play an important role in the regulation of tumor inflammatory responses and angiogenesis. Sub-clustering analysis of various myeloid cells in GC and normal gastric tissues (Fig. 5A) revealed mast cells (marked by *CPA3*), neutrophils (marked by *CXCR2*, *IL1R2*), monocytes (marked by *S100A9*, *EREG*, and *VCAN*), FOLR2_TAM (marked by *LYVE1* and *FOLR2*), TREM2_TAM (marked by *TREM2*), C1QC_TAM (marked by *C1QC*), VEGFA^{+}SPP1^{+} Angio-TAM (marked by *VEGFA* and *SPP1*), and three subsets of dendritic cells (DCs, marked by *CD1C*, *LAMP3*, *IDO1*, and *IRF8*) (Fig. 5, B and C, and fig. S3A). The proportion of TREM2_TAMs was significantly increased in HpGC and ex-HpGC, and Angio-TAMs was higher in HpGC tissues than in normal gastric tissues ($P < 0.05$, Student's t-test; Fig. 5D). TREM2_TAMs exhibited high expression levels of complement genes such as C1QA/C1QB/C1QC, which are predictive factors of prognosis, whereas Angio-TAMs expressed chemokines such as CXCL3, CXCL5, CXCL8, and IL1RN, which are involved in the immune escape (*33*) (Fig. 5E and table S5). Further signature enrichment analysis revealed that Angio-TAMs exhibited high expression levels of angiogenesis signature, whereas TREM2_TAMs exhibited a high level of M2 signature (Fig. 5F). Immunostaining revealed that Angio-TAMs were mainly located in the tumor vasculature, whereas TREM2_TAMs were mainly located in the tumor stroma (Fig. 5G). Furthermore, gene set variation analysis (GSVA) of upregulated genes revealed that TREM2_TAMs were enriched for PD1 signaling, innate immune system, and GC chemosensitivity, whereas Angio-TAMs were enriched for tumor angiogenesis, chemokines, HIF, VEGF pathway, and ECM organization involved in promoting the development of vascular and hypoxic tumors (Fig. 5H). Furthermore, we found that TREM2_TAMs and Angio-

262 TAM abundance were both highly correlated with Treg abundance (Fig. 5I and fig. S3B), which supports the
263 notion that TAMs play crucial roles in the modulation of Treg maturation and recruitment. Interestingly, the
264 intercellular crosstalk analysis revealed different ligand-receptor axes between TREM2_TAM-Tregs and Angio-
265 TAM-Tregs. The SPP1-CD44 axis and the "do not eat me" axis THBS1-CD47, which is an immune checkpoint
266 controlling $CD8^+$ T cell activation and immune escape, were mainly enriched in Angio-TAM and Tregs.
267 Additionally, we found Angio-TAM derived from HpGC or exHpGC showed higher expression of *THBS1*,
268 *VEGFA*, and *SPP1* than Angio-TAM of non-HpGC, and HC (fig. S3D). The immune checkpoint axes NECTIN2-
269 TIGIT, CD86-CD28, CD86-CTLA4, CXCL16-CXCR6, and LGALS9-HAVCR2 (TIM3) were exclusively
270 enriched in TREM2_TAM and Tregs (Fig. 5J and fig. S3C). Furthermore, the devolution analysis in TCGA bulk
271 GC transcriptome dataset revealed that the enrichment of Angio-TAMs was more significant in HpGC compared
272 with non-HpGC (P = 0.047, Wilcoxon test; Fig. 5K) and was associated with poor prognosis of GC (P = 0.0035,
273 log-rank test; Fig. 5L). Overall, our results revealed the heterogeneity and function differences of myeloid cells of
274 GC with different *H. pylori* infection status, and decipher distinct roles of TREM2_TAM and Angio-TAM
275 involved in gastric carcinogenesis and prognosis.

276 **Transcriptomic diversity of cancer-associated fibroblasts in *H. pylori* infection associated GC**

277 Cancer-associated fibroblasts (CAFs), another major component of the TME, not only produce ECM but also
278 secrete various molecules, including cytokines, chemokines, and growth factors, which are correlated with
279 migration, infiltration, and EMT, thereby playing a role in GC development and resistance to immunotherapy (*34*).
280 Therefore, we focused on the molecular characteristics of CAFs. CAFs can be divided into six subpopulations,
281 including three subsets of vascular-related CAF (vCAF) featuring the expression of microvasculature genes
282 MCAM, RGS5, and MYH11; and two subsets of matrix CAF (mCAF) characterized by high expression of
283 extracellular matrix (ECM) genes including *PDGFRA*, *LUM*, and *DCN* and inflammatory CAF (iCAF), which was
284 identified by high expression of *TWIST1*, *VEGFA* and inflammatory chemokine genes *CXCL5/8*, *IL11* (*35*), and
285 *IL24* (Fig. 6, A to C, fig. S4A, and table S6). Interestingly, iCAF shared highly consistent transcriptome phenotype
286 of iCAFs derived from human intrahepatic cholangiocarcinoma (fig. S4B) (*36*). The organization of the CAF
287 compartment showed great differences in GC with different *H. pylori* infection status (Fig. 6D) and the ratio of
288 iCAF was significantly higher in HpGC tissues than in normal gastric tissues (P = 0.023, Student's t-test; Fig. 6E)
289 and the ex-HpGC also showed an increase trend (P = 0.083, Student's t-test; Fig. 6E). Further enrichment analysis
290 revealed that iCAF enriched chemokines, TGFβ, ECM, IL6 pathway, PDGFRA pathway, inflammatory response,

291 hypoxia, tumor angiogenesis, and VEGF signaling pathway (Fig. 6F), which are crucial for tumor progression,
292 metastasis, and immune escape (*35*). Additionally, the abundance of iCAF significantly correlated with Angio-
293 TAM and suppressive Treg cells (Fig. 6G), the above results indicated an important role of iCAF in tumor TME
294 regulation and immune escape.

295 Further intercellular crosstalk analysis showed that iCAF had the strongest interaction with suppressive T cells
296 and TAM, indicative of complex roles in the TME (Fig. 6H). Specifically, the THBS, NECTIN, TIGIT, ANGPTL,
297 and VEGF signaling pathways were enriched in the cellular interplay between iCAF and suppressive T cells and
298 TAM (Fig. 6I). Detailed ligand-receptor crosstalk analysis showed that iCAF interacts with CD8_CXCL13, Tregs
299 mainly by NECTIN2-TIGIT ligand-receptor pair (Fig. 6I), which strongly implied that *H. pylori* infection
300 upregulates the expression of NECTIN2 in stromal cells that competitively bind to the TIGIT receptor on T cells,
301 leading to inhibition of T cell responses and immune escape of GC. In addition, angiogenesis-associated ligand-
302 receptor pairs such as VEGFA/B-VEGFR1 and ANGPTL4-SDC2 were mainly enriched between iCAF and Angio-
303 TAMs (Fig. 6I). Interestingly, we found iCAF derived from HpGC showed higher expression of *NECTIN2*,
304 *VEGFA*, *PVR* and inflammatory chemokine genes *IL11* and *IL24* compared to ex-HpGC, non-HpGC, and HC.
305 Additionally, we found that the elevated expression level of *IL11*, *VEGFA*, *IL24*, and *TWIST1* was correlated with
306 poor prognosis in GC ($P = 0.14$, $P < 0.05$, $P < 0.05$ and $P < 0.05$, respectively, log-rank test; fig. S4, C and D).
307 Furthermore, the validation results by virtue of two public GC bulk RNA datasets (*28, 29*) revealed that the
308 abundance of iCAF was elevated in HpGC samples than non-HpGC ($P = 0.035$, Wilcoxon test; Fig. 6J) and was
309 highly associated with poor prognosis in two public bulk transcriptomic dataset ($P = 0.12$ and $= 0.007$,
310 respectively, log-rank test; Fig. 6K). The above results indicated that iCAFs promoted tumor angiogenesis and
311 immune suppression in *H. pylori* infection associated GC, by upregulation of VEGFA/B-VEGFR1 pathway, and
312 NECTIN2-TIGIT pathway.

313 **The association of immune and stromal composition abundance with GC immunotherapy**

314 *H. pylori* infection has multiple immunomodulatory effects on the host, which can not only activate the immune
315 response but also negatively regulate it, causing immune escape. However, the key cell players and molecular
316 features for predicting the GC immunotherapy response remains largely unknown. To reveal the detailed molecular
317 features of the *H. pylori* infection associated GC TME for predicting the outcomes of immunotherapy, we
318 performed the devolution analysis to evaluate the cell type abundance, immune checkpoint, and angiogenic
319 signature expression in GC immunotherapy-treated bulk RNA sequencing dataset (*37*). GSEA and devolution

320 analysis demonstrated a high abundance of iCAF and Angio-TAM in anti-PD1 immunotherapy non-responsive
321 (NR) patients, while CD8_CXCL13, CD8_GZMB, CD8_IFNG and CD8_MKI67 were more abundant in anti-PD1
322 responsive cases (Fig. 7A and $P < 0.05$, Student's t-test; fig. S5A). The relative abundance of several cell clusters
323 such as CD8_CXCL13, CD8_MKI67 had a remarkable correlation with improved anti-PD1 overall survival (OS)
324 and progression-free survival (PFS), while the abundance of iCAF and Angio-TAM was significantly associated
325 with poor survival (Fig. 7, B and C). Furthermore, we defined an anti-PD1 immune signature and an angiogenic
326 signature (Fig. 7D and fig. S5B) derived from the cell type signatures of scRNA-seq result and found that the
327 immune signature was highly correlated with CD8_GZMK and CD8_GZMB, while the angiogenic signature
328 highly correlated with iCAF and Angio-TAM (fig. S5C). Interestingly, we found that the expression of immune
329 signature was higher in immunotherapy responsive GC cases than non-responsive cases, while the angiogenic
330 signature showed the oppositive trend ($P < 0.05$, Wilcoxon test; Fig. 7E). To better understand the cellular and
331 molecular characteristics that react to immunotherapy, we constructed a comprehensive model comprising cellular
332 composition and signature to evaluate the immunotherapy response of different parameters (fig. S5, D to F). The
333 results showed that immune signatures such as *CXCL13*, *LAG3*, *TIGIT*, and *PDCD1*, and cell types such as
334 CD8_CXCL13 and TREM2_TAM had high diagnostic power to distinguish between anti-PD1 responsive cases
335 and non-responsive cases (Area under the curve (AUC) > 0.75). Additionally, the immune signature we defined
336 also effectively distinguished anti-PD1 responsive cases from non-responsive cases to achieve better anti-PD1
337 immunotherapy prognosis (AUC = 0.755, Fig. 7F), whereas the angiogenic signature had poor diagnostic ability
338 for identifying anti-PD1 responses as well as poor anti-PD1 immunotherapy prognosis (AUC = 0.367, Fig. 7F).
339 Further Kaplan-Meier survival analysis revealed that the defined immune signature was correlated with better
340 immunotherapy efficacy in terms of OS and PFS in GC while the angiogenic signature linked with poor
341 immunotherapy response ($P < 0.05$, log-rank test; Fig. 7G and fig. S5G). In brief, by integrating our single-cell
342 transcriptional results of GC with public bulk RNA-seq data of immunotherapy-treated GC, we identified several
343 cell types and molecules that could serve as indicators to predict the immunotherapy response of GC, thus flagging
344 up individualized GC therapy.
345
346 **DISCUSSION**
347 GC is the third most common tumor in Asia and is mainly caused by *H. pylori* infection. Numerous studies had
348 shown that *H. pylori* infection not only leaded to GC but also affected the TME of GC and response to

349 immunotherapy (*5, 13, 38, 39*). Owing to advances in scRNA-seq, the heterogeneity of cell components in the
350 TME of human malignancies can be elucidated. In this study, we profiled the single-cell transcriptional
351 characteristics of the TME of GC tissues to reveal the role of *H. pylori* infection in GC development, TME
352 regulation, and immunotherapy response. Specifically, we revealed the TME transcriptomic phenotype and
353 composition, functional features, and potential intercellular interactions of GC with different *H. pylori* infection
354 status, which provided evidence and biomarkers for predicting the prognosis of immunotherapies for *H. pylori*
355 infection associated GC.

356 First, we used inferCNV algorithms to distinguish non-malignant epithelium from the malignant epithelium and
357 found that malignant epithelium derived from *H. pylori* associated GC exhibited inflammation and EMT
358 signatures, which provided potential biomarkers for the diagnosis of *H. pylori* infection associated GC (*40*). We
359 also revealed that *H. pylori* infection leads to dramatic loss or death of parietal cells and delineated the
360 development trajectory of gastric chief cells along the cascade GC at the single-cell level, which broadened our
361 previous findings to reveal the chief cell transitions (*23*). Based on the expression pattern of signature genes and
362 TFs, we found that chief cells could give rise to neck cells; subsequently, SPEM then showed distinct branches,
363 and only part of SPEM developed into intestinal-specific cell types, including IM and enterocytes, under
364 conditions of chronic inflammation, which further validates the evolutionary path of the non-malignant epithelium
365 of GC under *H. pylori* infection.

366 Next, we evaluated the heterogeneity and molecular features of immune and stromal components among the
367 TME of normal and all GC tissue and found that HpGC tissues were enriched with iCAF, Angio-TAM, TREM2^{+}
368 TAM and suppressive T cells, and that iCAF was highly linked to Angio-TAM and suppressive T cells, also the
369 abundance of iCAF is associated with poor immunotherapy efficacy. Intercellular crosstalk analysis revealed that
370 iCAF and TREM2^{+}TAM interacted with suppressive T cells: Treg and CXCL13^{+}CD8 via the NECTIN2-TIGIT
371 pathway. Previous studies had shown that *H. pylori* infection upregulates PD-L1 expression in a variety of cells,
372 including TAM, eosinophils, and dendritic cells (*13, 19, 41*). PD-L1 upregulation in these cells may compete with
373 PD-1 binding to T cells, thereby inhibiting T cell responses, and affecting the therapeutic efficacy of PD-1/PD-L1
374 inhibitors (*42, 43*). The above results indicated that *H. pylori* infection could upregulate NECTIN2 expression in
375 immune and stromal components, which mediated immune escape and impairs immunotherapy efficacy. Hence,
376 inhibition of the TIGIT-NECTIN2 axis may be a promising treatment strategy in HpGC.

377 *H. pylori* infection impairs the efficacy of anti-PD-1/CTLA4 immunotherapies or anti-cancer vaccines, and a

lack of efficient targets impedes the treatment of *H. pylori* infection associated GC (*5*). However, the key cellular players and signaling pathways involved in the association of *H. pylori* infection with immunotherapy efficacy remain poorly investigated. In this study, iCAFs exhibited upregulation of angiogenic molecules VEGFA/B and ANGPTL, with the highest expression levels identified in cells derived from HpGC. Additionally, iCAFs were notably enriched in tumor angiogenesis, ECM, TGFβ, and VEGF pathway, our results also showed that iCAFs could interact not only with immunosuppressive T cells through the NECTIN2-TIGIT and THBS1/2-CD47 axes, but also with Angio-TAMs through the VEGFA/B-VEGFR1 and ANGPTL-SDC2 axes. These results indicated an important role of iCAFs in stromal TME regulation, immune escape, and tumor angiogenesis. Recent research displayed that block of placental growth factor (PIGF), a member of the vascular endothelial growth factor, could inactive CAFs and reduce the deposition of fibrosis-associated collagen and desmoplasia in pancreatic cancer TME, which could improve survival rate of murine pancreatic ductal adenocarcinoma (PDAC) model. Furthermore, PD-L1 directed PIGF/VEGF block by fusing of single chain of anti-PD-L1 antibody (atezolizumab) to VEGF-Grab could target PD-L1-expressing CAF thus promote anti-fibrotic and anti-tumor effect (*44*). As we know, CAFs can shape the ECM, and form a barrier for drug or therapeutic immune cell penetration, which prevents the deep penetration of drugs and immune cells into tumor tissues, thereby reducing the effectiveness of treatments. Therefore, inhibition of tumors by modulating CAFs or overcoming their barrier effects is a new therapeutic strategy. Taken together, our findings were consistent with those of previous ones that had hypothesized that anti-angiogenic targeted therapy could augment antitumoral immunity and enhance immunotherapy efficacy by targeting tumor angiogenesis, exhausted T cells proliferation and myeloid cell inflammation(*45-48*).

This study has some limitations and the main findings should be validated in a large patient cohort. Secondly, our findings were mainly based on scRNA-seq and bioinformatic analysis, only a small number of key molecules and cell types have been verified by immunostaining, additionally, we conducted deconvolution analysis using external datasets to further validate our results. Even these validations provide support at genomic and protein level, it is important to note that functional validation is still lacking. Further clinical trial research should be performed to validate the efficacy of combination immunotherapy alone or in combination with anti-VEGF therapy in *H. pylori* infection associated GC. Nevertheless, we provided vital insights into the molecular and cellular heterogeneity of *H. pylori* associated GC at a single-cell level. Moreover, the enrichment of the TIGIT-NECTIN immune checkpoint and angiogenesis signaling pathways in different cell types in the TME of *H. pylori*

407 infection associated GC implies that the potential combination of immunotherapies and anti-angiogenic targeted
408 therapeutic modalities could be an effective therapeutic approach for *H. pylori* infection associated GC.
409
410 **Materials and methods**
411 **Ethics approval:**
412 The study was conducted according to the guidelines of the Declaration of Helsinki and approved by the Ethics
413 Committee of Fourth Medical Center of PLA General Hospital. (2021KY011-HS001, 2021KY041-HS001) All
414 study participants provided written informed consent.
415
416 **Acquisition of fresh tissue materials and preparation of single cell suspension**
417 Normal gastric tissue biopsy specimens were obtained from 2–3 gastric antrum sites through conventional upper
418 gastrointestinal endoscopy using biopsy forceps. GC tissues were obtained immediately after surgical resection
419 with a scalpel. The fresh tissue samples were then washed with phosphate-buffered saline (PBS) and divided into
420 two parts. One part was processed into a single cell suspension, and the second part was used for other
421 experiments, including the detection of *H. pylori* DNA, H&E and immunofluorescence staining. The patients'
422 serum was used to detect the IgG antibody of *H. pylori*. Patients with positive serum antibody and genomic DNA
423 of *H. pylori*, and *H. pylori* observed on H&E slides, were defined as GC patients with current *H. pylori* infection
424 (HpGC). Patients with positive serum antibody but negative genomic DNA had a history of *H. pylori* eradication
425 or antibiotic use before surgery, and *H. pylori* cannot be observed on H&E slides. They were defined as GC
426 patients with previous *H. pylori* infection (ex-HpGC). The negative detection of serum antibody and genomic
427 DNA, as well as H&E, indicated that the volunteers never had *H. pylori* infection, which was defined as GC
428 patients or healthy volunteers without *H. pylori* infection (non-GC and HC).
429 The biopsy and surgical samples used to prepare the single cell suspension were immediately put into a tissue
430 preservation solution (Miltenyi Biotec, Germany) and transported to the field laboratory in an ice bath for
431 immediate preparation of the single cell suspension. Fresh tissue samples were washed with 4 °C precooled
432 Dulbecco's Phosphate-Buffered Salines (DPBS, Solarbio, Beijing) for 2–3 times, cut into small pieces with
433 surgical scissors, and then transferred to a 1.5 ml centrifuge tube. The tissue samples were incubated in a shaker at
434 37 °C for 30–50 min with an in-house prepared enzymolysis solution (1 mg/ml type IV collagenase (Solarbio,
435 Beijing) + 10 U/μL DNase I DNase I (Roches)) or MACS Human Tumor Dissociation kit (DS_130-095-929,

436 Miltenyi Biotec, Germany). The incubation was terminated when the digestive fluid turned turbid and the tissue
437 block disappeared. The cell suspension was filtered with a 40-μm cell sieve and centrifuged at 4 °C at 300 r/min
438 for 5 min. After the supernatant was discarded, the cells were resuspended in 1 ml of DPBS, and 3 ml of precooled
439 red blood cell lysate (Solarbio, Beijing) were added. The cells were evenly aspirated, incubated at 4 °C for 5–10
440 min, and centrifuged again. The cells were stained with 7-Aminoactinomycin D (7-AAD, eBiocience, Cat# 00-
441 6993-50) staining solution (100 μL 1% BSA/PBS + 5 μL 7-AAD) at 25 °C for 5 mins. Consequently, the
442 individual cells with high quality were sorted by FACS performed with a BD Aira II instrument and checked by
443 staining them with trypan blue under the microscope for single cell transcriptomic library construction.
444
445 **Detection of *H. pylori* nucleic acid in the gastric mucosa**
446 *H. pylori* in human gastric mucosa was detected using a *H. pylori* nucleic acid detection kit (PCR-fluorescent
447 probe method, Daan Gene, Guangzhou, China), according to the manufacturer's protocols. Briefly, the following
448 steps were performed: (1) DNA extraction: DNA extraction solution was added to the negative/positive quality
449 controls and the samples to be tested. The solutions were treated at a constant temperature of 100 °C for 10 min,
450 and centrifuged at 12,000 r/min for 5 min for later use; (2) Fluorescence PCR: 2 μL samples were briefly
451 centrifuged at 8,000 r/min and then placed in a PCR machine, 50°C for 8 min, 93°C for 2 min, 93°C for 45
452 s→55°C for 1 min (10 cycles), 93°C for 30 s→55°C for 45 s (30 cycles), and 50°C for 45 s to collect fluorescence
453 values. The system automatically analyzed the results to calculate the threshold cycle value (CT value); (3) Quality
454 control and results calculation: the fluorescence signal of the negative control material did not increase, the growth
455 curve of the positive control material was S-shaped, and the Ct value was ≤27.04. The sample results were
456 compared to those of the quality control material. *H. pylori* cagA was detected with the Nucleic acid test kit of *H.*
457 *pylori* type I (fluorescent PCR method, Beijing Xinji Yongkang, China), and the method was carried out according
458 to the manufacturer's protocols.
459
460 **Detection of serum antibody against *H. pylori***
461 *H. pylori* IgG ELISA kit (IBL, Germany) was used to detect the presence of anti-*H. pylori* antibodies in the serum
462 of the subjects following the manufacturer's instructions. The cut-off index (COI) was determined by dividing the
463 optical density (OD) value of the sample by the OD value of cut-off standard. The cut-off index (COI) was
464 determined by dividing the optical density (OD) at 450nm value of the sample by the OD_{450} value of cut-off

standard. The serum was considered positive for *H. pylori* if the COI was > 1.2, while the serum was considered negative if the COI < 0.8.

Single-cell sequencing and pre-processing data

We prepared single-cell RNA-seq libraries on the Chromium platform (10× Genomics, Pleasanton, CA, USA) using the Chromium Next GEM Single-Cell 3' Kit v2 following the manufacturer's protocol to generate a complementary deoxyribonucleic acid (cDNA) library in Biomarker Technologies and Capitalbio Technology Corporation (China). Briefly, viable cells (7-AAD negative) with high quality were pooled together and washed thrice with RPMI-1640, concentrated to 700−1000 cells per μL, and then immediately loaded onto a 10× microfluidic chip (10× Genomics) to generate single cell mRNA libraries and then sequenced across six lanes on an Illumina X ten or NovaSeq 6000 system (Illumina, Inc., San Diego, California, US). Raw sequencing data were aligned to the GRH38 reference genome using cellranger (10× Genomics, v4) count function. The count matrixes of gene expression from each sample were imported into the Seurat(*49*). We selected high-quality cells for further analysis following three measurements: (1) cells had either over 2001 unique molecular identifiers (UMIs), fewer than 6,000 or more than 301 expressed genes or fewer than 20% UMIs derived from the mitochondrial genome; (2) genes expressed in more than ten cells in a sample; (3) cell doublets were removed using the DoubletFinder R package(*50*). The cell-by-gene expression matrixes of the remaining high-quality cells were integrated with the RunFastMNN function provided by the SeuratWrappers R package and then normalized to the total cellular UMI count. The union of the top 2,000 genes with the highest dispersion for each dataset was used to generate an integrated matrix. We then performed data normalization, dimension reduction, and cluster detection as previously reported(*23*). Briefly, the gene expression matrixes were scaled by regressing the total cellular UMI counts and percentage of mitochondrial genes. Principal component analysis (PCA) was conducted using highly variable genes (HVGs), and the top 30 significant principal components (PCs) were selected to perform uniform manifold approximation, projection (UMAP) dimension reduction, and visualization of gene expression. We annotated cell sub-clusters with similar gene expression patterns as the same cell type, and cell types in the resulting two-dimensional representation were annotated to known biological cell types using canonical marker genes.

Detection of single-cell CNVs

We employed the inferCNV(*51*) R package (https://github.com/broadinstitute/inferCNV/wiki) to distinguish

494 malignant and non-malignant epithelia of GC, and the initial CNV signal of each region was estimated based on
495 the expression level from the scRNA-seq results with default parameters.
496
497 **Pathway enrichment and cell type abundance deconvolution analysis**
498 To illustrate the enriched signaling pathways of fibroblast and myeloid subtypes, we used the GSVA(*52*) package
499 to assess pathway differences using the C2 curated gene set provided by the Molecular Signatures Database
500 (MSigDB), which were calculated with a linear model offered by the limma package. We used the GSVA(*52*)
501 package to calculate the abundance of malignant epithelium subclusters in *H. pylori* positive GC using the
502 TCGA(*29*) and Asian Cancer Research Group (ACRG) cohorts(*28*). We used GSEA package to calculate the
503 distribution of gene sets and cell-type-specific signatures (top 30 DEGs) in lists of genes ordered by population
504 expression differences. Normalized enrichment score (NES).
505
506 **Malignant epithelium differentiation score**
507 To assess the malignant epithelium differentiation heterogeneity at single cell level, we included a tumor
508 differentiation associated signature to evaluate the GC differentiation heterogeneity based on our previous study
509 (*23*) , including PHGR1, MUC13, MDK, KRT20, LGALS4, GPA33, CLDN3, CLDN4, and CDH17, and then we
510 employed the "AddModuleScore" function of Seurat R package to calculate the differentiation degree of each
511 tumor cell based on the expression level of differentiation associated signature.
512
513 **TCGA data analysis**
514 For the analysis of the correlation of tumor differentiation score and cell subtypes abundance with patients' clinical
515 outcome, we employed the GSVA to calculate the differentiation score and cell subtypes abundance in each TCGA
516 stomach adenocarcinoma (STAD) sample based on the tumor differentiation signature and the top 30 DEGs of
517 each cell subtype, and then grouped samples into high and low groups based on 67th and 33th percentile
518 respectively(*53*). Kaplan-Meier survival curves were plotted using the R package "survminer".
519
520 **Immunotherapy response and prognosis analysis**
521 GC immunotherapy bulk RNA-seq data along with curated clinical data from patients were obtained from a
522 previous study (*37*). To evaluate the association between the signatures of immune and stromal subtypes identified

523 in our study and immunotherapy response to GC patient survival, the GSVA (*52*) was used to calculate the
524 combined expression value of the cell-type-specific signatures (top 30 DEGs). We classified the patients into high
525 and low groups based on the 50th and 50th of cell subtypes abundance. Kaplan-Meier survival curves were plotted
526 using the R package "survminer". Subsequently, a Cox proportional hazards model has conducted that included
527 age and tumor stage. The results of the Cox regression model among the cell subtypes were visualized using
528 weighted Z-scores.
529
530 **Trajectory analysis**
531 To explore the potential differentiation routines between the non-malignant epithelium of GC, we performed
532 trajectory analysis using the monocle R package as previously reported (*54*). First, we constructed the monocle
533 object using the "newCellDataSet" function, and the differentially expressed genes calculated via the
534 "differentialGeneTest" function were selected for trajectory analysis. Then "DDRTree" function was used for
535 dimensionality reduction and the "plot_cell_trajectory" function for visualization.
536
537 **Intercellular crosstalk**
538 We used the Cellchat(*55*) package (v0.0.2) to infer the intercellular communications and significant ligand-
539 receptor pair of the *H. pylori* infection associated GC TME, following a standard pipeline implemented in R
540 (https://github. com/sqjin/CellChat). We first set the ligand-receptor interaction list in humans and projected the
541 gene expression data onto the protein-protein interaction (PPI) network by identifying the overexpressed ligand-
542 receptor interactions. To obtain biologically significant cell-cell communication, the probability values for each
543 interaction were calculated by performing permutation tests. The inferred intercellular communication network of
544 each ligand-receptor pair and each signaling pathway was summarized and visualized using circle plots and
545 heatmaps.
546
547 **Multi-labelled immunofluorescence staining and multispectral imaging**
548 A PANO 7-plex IHC kit (cat 10004100100; Panovue, Beijing, China) was used to perform multiplexed
549 immunofluorescence staining. Slides were placed in a 65 °C oven overnight to for deparaffinization, and tissues
550 were sequentially treated with xylene, ethanol, and distilled water. Slides were then microwaved (with antigen
551 retrieval solution [citric acid solution, pH6.0/pH9.0]) and sequentially incubated with different primary antibodies

and horseradish peroxidase-conjugated secondary antibodies (100 μL/tissue, table S7). This incubation was followed by tyramide signal amplification (TSA Fluorescence Kits, Panovue, Beijing, China). The slides were washed with 1× PBST after each incubation and microwaved after each round of TSA. After all the antigens were labelled, the nuclei were stained with 4'-6'-diamidino-2-phenylindole (DAPI, Sigma-Aldrich, MO, USA). Stained slides were scanned using a Mantra system (PerkinElmer, Waltham, Massachusetts, USA) to obtain multispectral images.

Abbreviations used in this paper: GC, gastric cancer; *H. pylori, Helicobacter pylori;* HC, healthy control; non-HpGC, gastric cancer without *H. pylori* infection; HpGC, gastric cancer with current *H. pylori* infection; ex-HpGC, gastric cancer with previous *H. pylori* infection; CAF, cancer-associated fibroblasts; iCAF, inflammatory CAF; Vcaf, vascular-related CAF; mCAF, matrix CAF; EMT, epithelial-mesenchymal transition; Angio-TAM, angiogenic tumor-associated macrophages; TME, tumor microenvironment; ICIs, Immune checkpoint inhibitors; scRNA-seq, single-cell RNA sequencing; VEGFR, VEGF receptor; TIGIT, T cell immunoreceptor with Ig and ITIM domains; FACS, fluorescence-activated cell sorting; CNV, copy number variation; GO, Gene ontology; SPEM, spasmolytic polypeptide-expressing metaplasia; IM, intestinal metaplasia; TFs, transcription factors; TILs, Tumor infiltrating lymphocytes; NK, natural killer; ECM, extracellular matrix.

Acknowledgments: We thank all patients enrolled in this study. All authors declare that they have no competing interests. **Funding:** This research was funded by National Science and Technology Major Project for Prevention and Treatment of Infectious Diseases (2018ZX10101003-005-005), and this study was also supported by grants from National Natural Science Foundation of China (82203636) and Young Talent Project of Chinese PLA General Hospital (20230403). **Author contributions:** CL, MZ, YW and SY were responsible for the study concept, design, interpretation and revising the manuscript. XZ, GZ, SS, YF and XC designed the experiments, collected the biopsies, analyzed the data, and wrote the manuscript. FL, JC, SR, and LP collected the biopsies. WS, HT and QG collected the biopsies, analyzed the data. HW and LZ evaluated gastric tumor pathology. **Competing interests:** The authors declare that they have no competing interests. **Data and materials availability:** The processed scRNA-seq data required to reproduce the analysis and figures have been deposited on Zenodo, which can be accessed with link https://zenodo.org/record/8082331. The TCGA GC bulk RNA-seq expression data was downloaded from the UCSC Xena website (https://xenabrowser.net/) and the GC immunotherapy expression

matrix data can be accessed in European Nucleotide Archive with accession PRJEB25780. Other GC bulk RNA and microarray data used in this study are available in the NCBI database under accession code GEO accession numbers GSE62254, and GSE2669. All data needed to evaluate the conclusions in the paper are present in the paper and/or the Supplementary Materials

Figure Legends

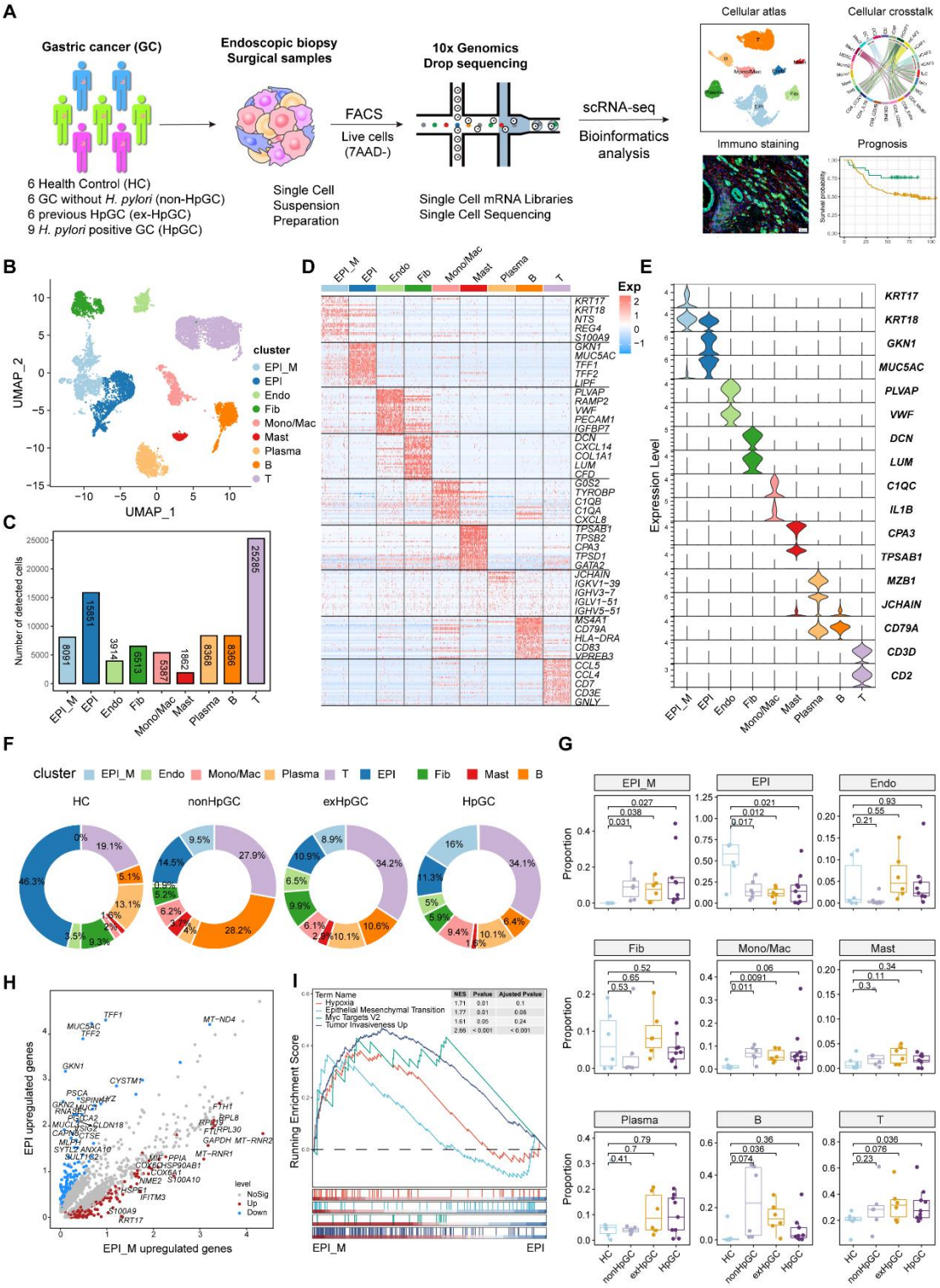

Fig. 1 Global analysis of the tumor microenvironment and malignant features of *H. pylori* infection associated GC. (A) A general workflow of GC sample preparation and processing of single-cell suspensions for scRNA-seq analysis. In total, 27 gastric samples, including gastric tissues of healthy control (HC, n=6), gastric cancer without *H. pylori* infection (non-HpGC, n=6), gastric cancer with previous *H. pylori* infection (ex-HpGC, n=6) and gastric cancer with current *H. pylori* infection (HpGC, n=9), were collected to perform scRNA-seq. (B)

593 Uniform Manifold Approximation and Projection (UMAP) plot for unbiased clustering and cell type annotation of
594 86,637 high-quality cells. EPI_M: malignant epithelium; EPI: non- malignant epithelium; Endo: endothelium; Fib:
595 fibroblast; Mono/Mac: monocyte/macrophage; Plasma: plasma cells; Mast: mast cells; B: B cells; T: T cells. (C)
596 the absolute quantities of nine different cell types. (D) Heatmap showing the top eight differentially expressed
597 genes (DEGs) of nine main cell types. (E) Violin plots showing the expression of signature genes of nine cell
598 types. (F) Pie plot revealing the proportions of nine cell types in HC, non-HpGC, ex-HpGC and HpGC. (G) Box
599 plot showing statistical analysis of proportion of nine cell types in HC, non-HpGC, ex-HpGC and HpGC. The *P*
600 value of Student's t test is shown. (H) Volcano plot displaying the differential upregulated genes in EPI and
601 EPI_M. (I) GSEA showing the pathway activity (scored per cell by Gene Set Enrichment Analysis) in malignant
602 epithelium (EPI_M) and non-malignant epithelium (EPI).

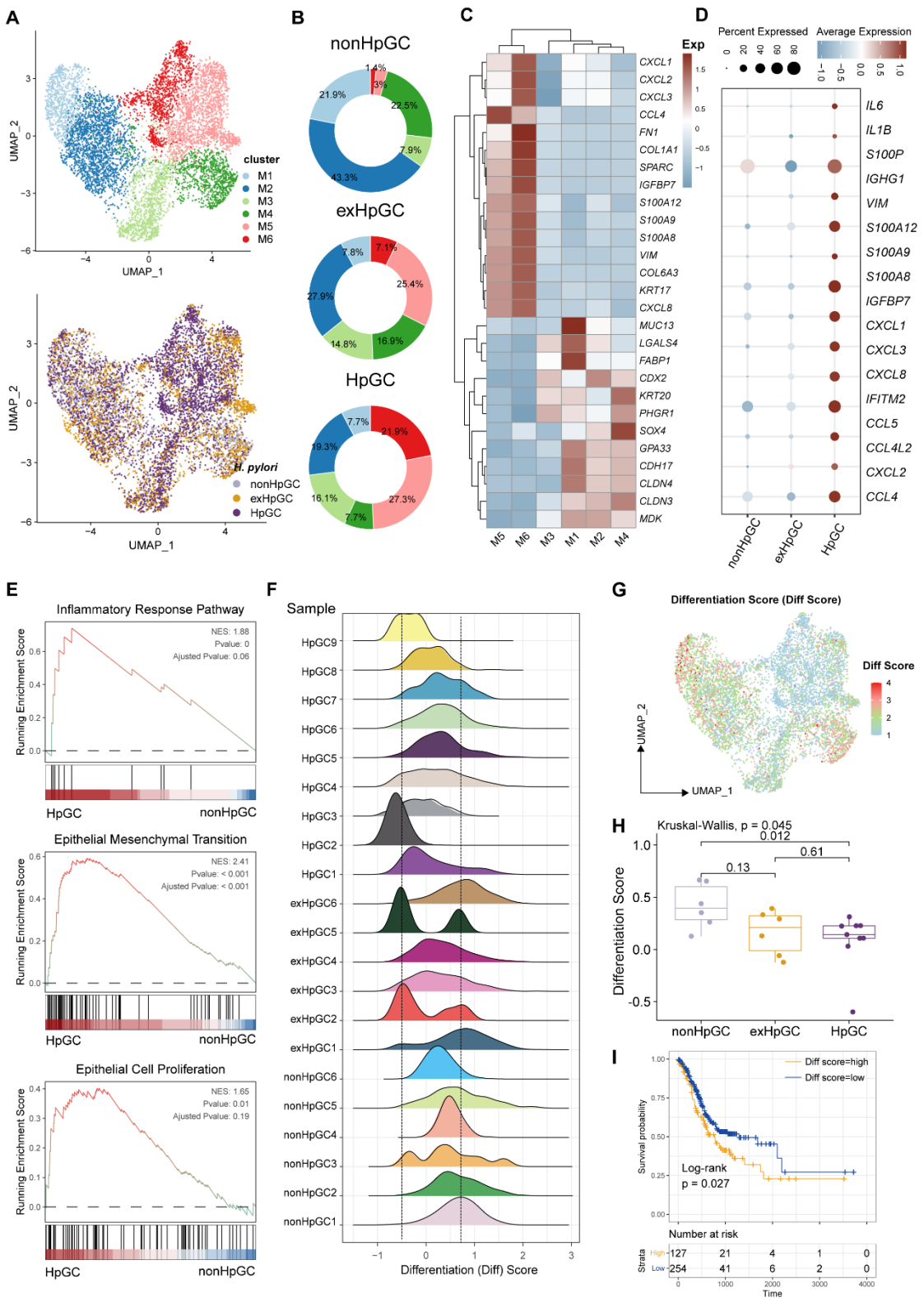

Fig. 2 Characterization of the malignant epithelium within GC with different *H. pylori* infection status. (A) UMAP plot showing six subpopulations of malignant epithelium, colored by different cell types (upper) and different *H. pylori* infection status (lower). (B) Pie plot showing the proportion of six subset of malignant epithelium in non-HpGC, ex-HpGC, and HpGC. (C) Heatmap displaying the differentially expressed genes

608 (DEGs) among the six subsets of malignant epithelium. (D) Bubble plot showing the difference of representative
609 molecular among the non-HpGC, ex-HpGC, and HpGC. (E) GSEA showing the pathway activity (scored per cell
610 by Gene Set Enrichment Analysis) in malignant epithelium of HpGC compared to that of nonHpGC. NES,
611 normalized enrichment score. (F) The ridge plot showing the differentiation score (Diff Score) of malignant
612 epithelium within each sample. (G) Heatmap showing the Diff Score of six subpopulations of malignant
613 epithelium. (H) Box plot showing differentiation score among non-HpGC, ex-HpGC, and HpGC, *P* values were
614 assessed by Wilcoxon test, Two-way ANOVA test is used for comparison of multiple groups. (I) Kaplan-Meier
615 survival analysis of TCGA STAD patients stratified by tumor sample differentiation scores, which was used to
616 group samples into high and low groups based on 33th and 67th percentile. The *P* value of two-sided log-rank test is
617 shown.

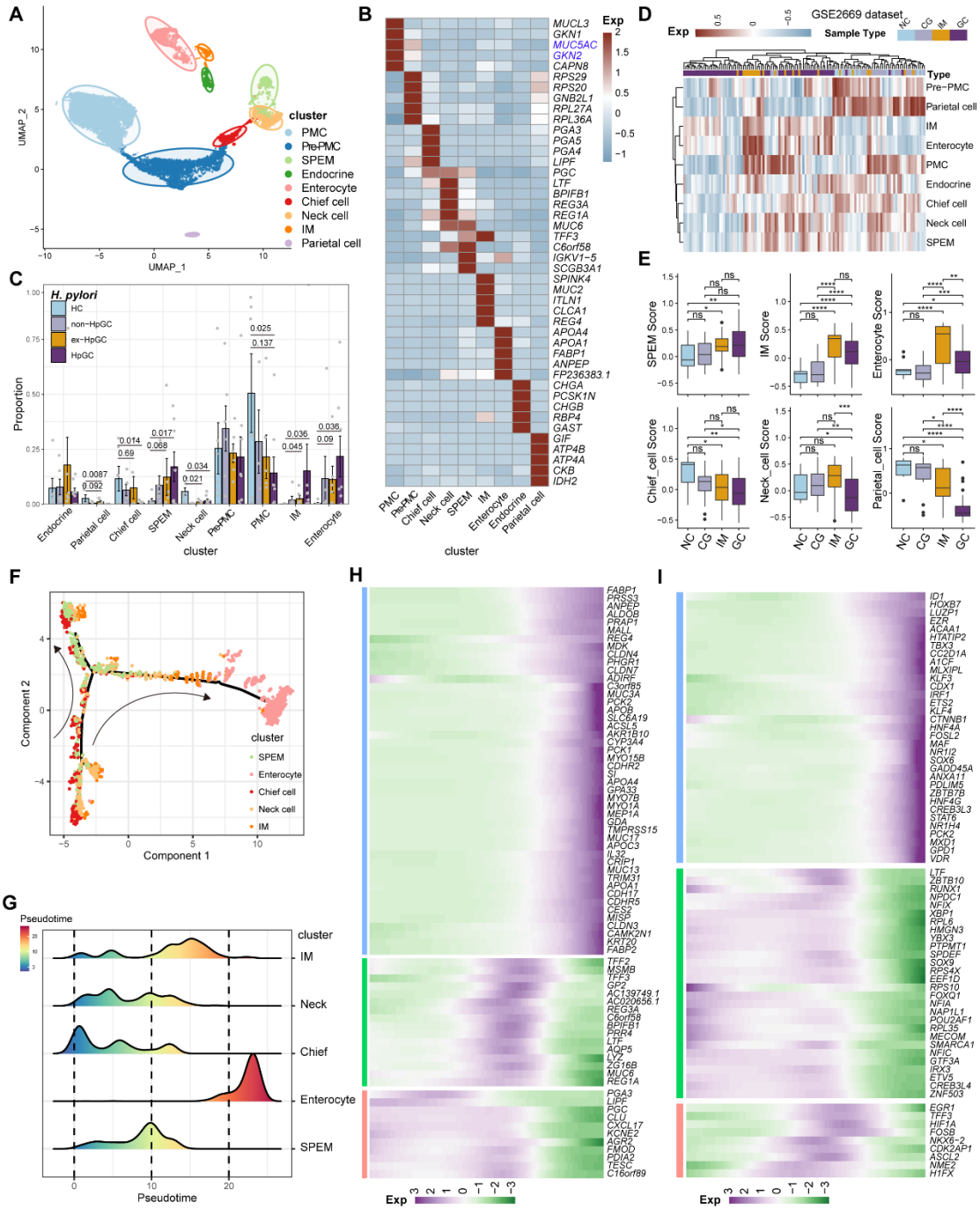

Fig. 3 Characterization of the non-malignant epithelium within GC with different *H. pylori* infection status. (A) Unbiased clustering of non-malignant epithelium generated nine subtypes. (B) Heatmap showing the molecular feature of non-malignant epithelium according to the top five DEGs. (C) Box plot showing the dynamic proportion of different cell types in non-malignant epithelium with different *H. pylori* infection status. (D) Heatmap showing the relative abundance (estimated by GSVA) of non-malignant epithelium subtypes in normal control (NC), chronic gastritis (CG), intestinal metaplasia (IM), GC samples (GSE2669). (E) Boxplot showing the relative abundance (estimated by GSVA) of non-malignant epithelium subtypes SPEM, IM, Enterocytes, Chief

cells, Neck cells and Parietal cells within NC, CG, IM, and GC samples (GSE2669). The *P* value of Student's t test is shown. (F) The trajectory analysis showing potential differentiation and transition trajectories in non-malignant epithelium clusters. (G) The ridge plot showing the pseudotime of non-malignant epithelium revealed the gastric pre-lesion process. (H–I) Heatmap showing scaled expression of dynamic genes (G) and TFs (H) along cell pseudotime.

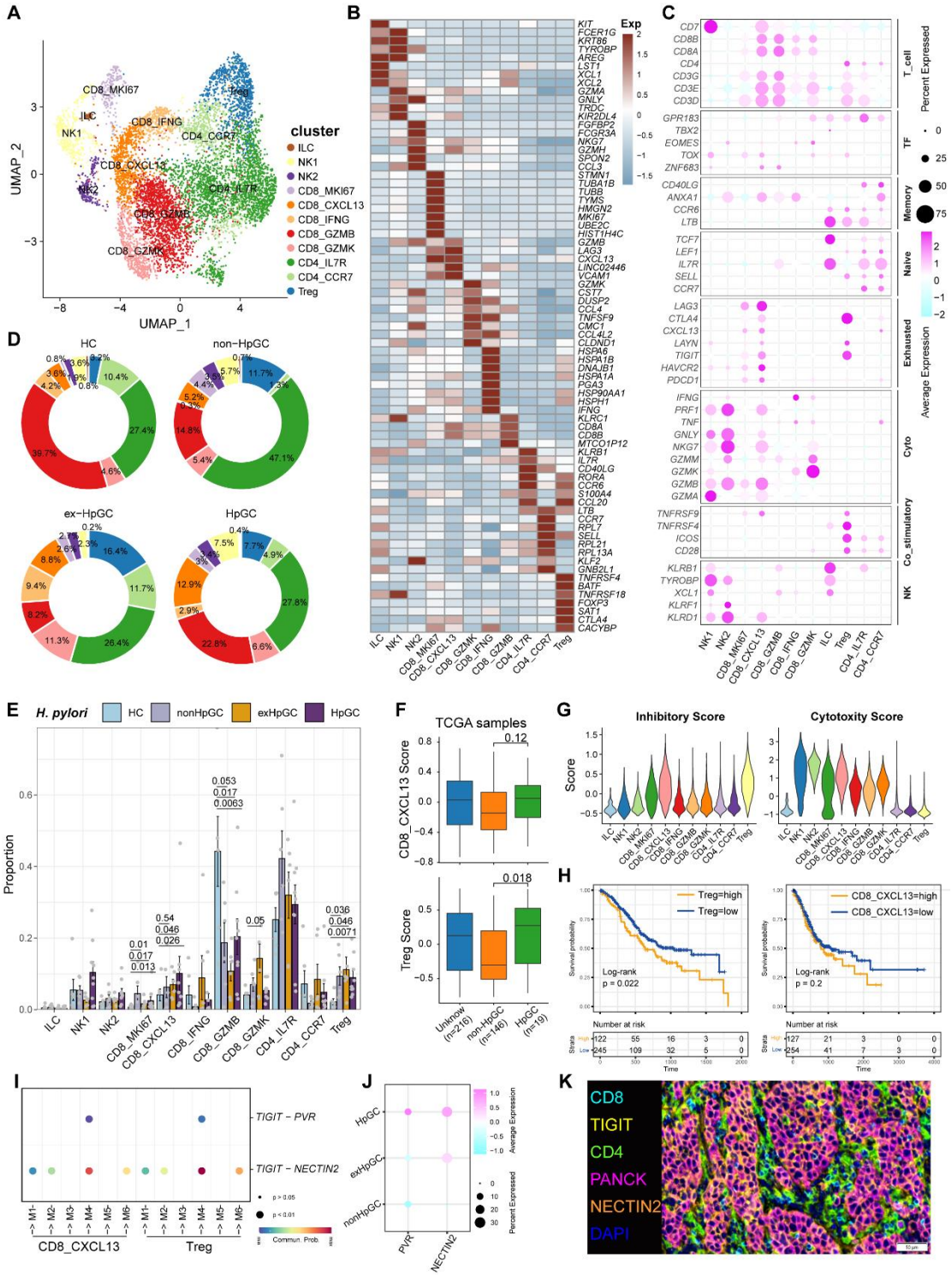

632 **Fig. 4 Characterization of tumor-infiltrating T and natural killer (NK) cells in *H. pylori* infection associated**
633 **GC.** (A) Unbiased clustering of T and NK cells generated 11 clusters. (B–C) Molecular features annotations
634 according to the top five DEGs (B), and representative genes (C). (D) Pie plot showing the T/NK cell subtype
635 abundance distribution in HC, non-HpGC, ex-HpGC, and HpGC. (E) The percentage contribution of T/NK cell
636 subtype in HC, non-HpGC, ex-HpGC, and HpGC samples. *P* values were assessed by Student t test. (F) The
637 deconvolution analysis showing the relative abundance of CD8_CXCL13 and Tregs in GC with different *H. pylori*
638 infection status with TCGA STAD dataset, *P* values were assessed by Wilcoxon test. (G) The cytotoxic and
639 inhibitory expression scores in T and NK clusters. (H) Kaplan-Meier survival analysis of TCGA STAD patients
640 stratified by CD8_CXCL13 and Tregs relative abundance, which was used to group samples into high and low
641 groups based on 33th and 67th percentile. The *P* value of two-sided log-rank test is shown. (I) Bubble plot showing
642 intercellular interactions between suppressive T cells and malignant cells. (J) Dotplot showing the expression of
643 NECTIN2 and PVR in malignant non-HpGC, ex-HpGC, and HpGC cells. (K) Immunostaining showing the ligand
644 TIGIT expressed in suppressive T cells and the receptor NECTIN2 expressed on the malignant epithelium,
645 respectively, in one HpGC sample.

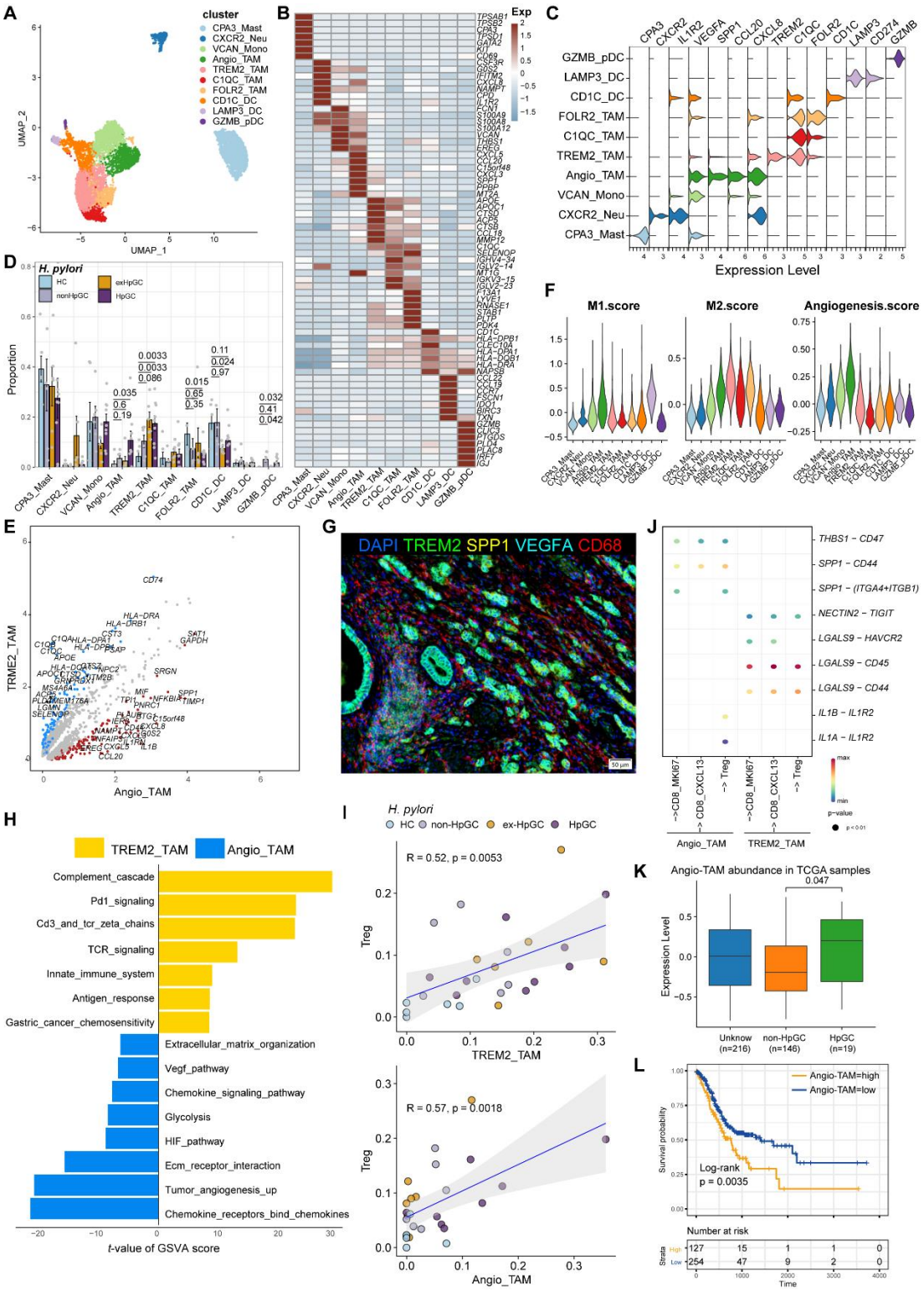

Fig. 5 Characterization of tumor-infiltrating myeloid cells by scRNA-seq in *H. pylori* infection associated GC. (A–C) Unbiased clustering of myeloid cells generated nine clusters (A), and molecular features were annotated according to the top seven DEGs (B) and representative genes (C). (D) The percentage contribution of each myeloid cells cluster in HC, non-HpGC, ex-HpGC, and HpGC. *P* values were assessed by Student t test. (E) Volcano plot showing the DEGs between Angio-TAM and TREM2^{+} TAM. (F) Violin plot showing the expression

652 of functional gene sets in myeloid clusters. (G) Immunostaining showing the distribution of Angio-TAM and
653 TREM2^{+} TAM in one HpGC sample. (H) Barplot showing the enriched signaling pathway between Angio-TAM
654 and TREM2^{+} TAM. (I) The correlation of cell type (percentage) between Tregs and Angio-TAM and TREM2^{+}
655 TAM. (J) Dotplot showing intercellular interactions among suppressive T cell and Angio-TAM and TREM2^{+} TAM.
656 (K) The relative abundance of Angio-TAM in HpGC and non-HpGC in TCGA STAD dataset, *P* values were
657 assessed by Wilcoxon test. (L) Kaplan-Meier survival analysis of TCGA STAD patients stratified by Angio-TAM
658 relative abundance, which was used to group samples into high and low groups based on 33th and 67th percentile.
659 The *P* value of two-sided log-rank test is shown.

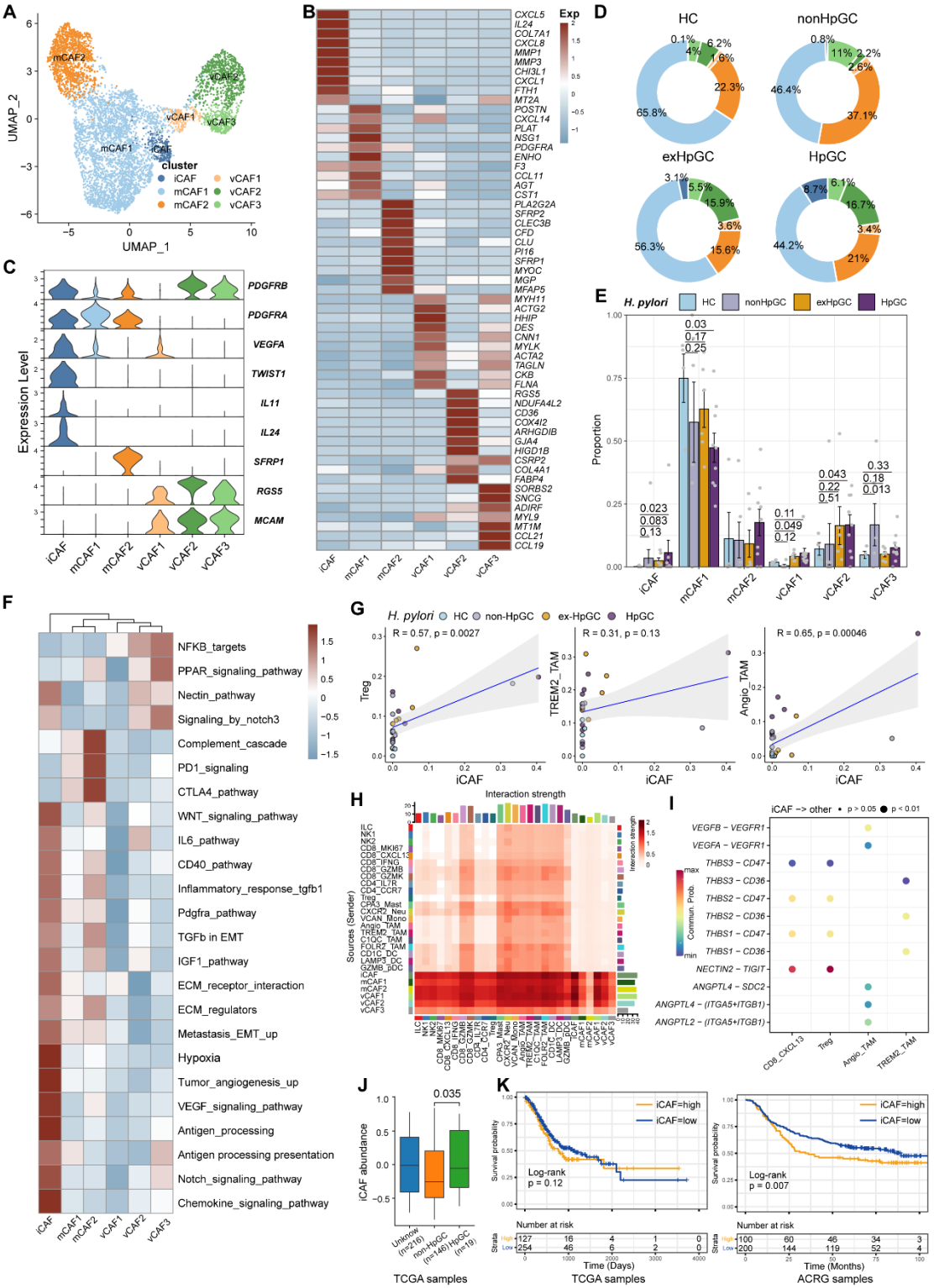

Fig. 6 Characterization of cancer-associated fibroblasts (CAFs) by scRNA-seq in *H. pylori* infection associated GC. (A) Unbiased clustering of CAF generated 6 clusters. (B–C) Molecular features annotations according to the top ten DEGs (B) and representative genes (C). (D) The pie plot showing the abundance distribution of six CAF subset in HC, non-HpGC, ex-HpGC, and HpGC. (E) The percentage contribution of each CAF cluster in HC, non-HpGC, ex-HpGC, and HpGC. *P* values were assessed by Student t test. (F) Heatmap

showing the enriched signaling pathway among six CAF clusters. (G) The cell type percentage correlation between iCAF and Treg, Angio-TAM, and TREM2^{+} TAM. (H) Heatmap showing intercellular interaction strength among immune cells and different subsets of CAF. (I) Enriched signaling pathway among suppressive T cell, Angio-TAM, and TREM2^{+} TAM with iCAF. (J) The relative abundance of iCAF in HpGC and non-HpGC in TCGA STAD dataset. *P* values were assessed by Wilcoxon test. (K) Kaplan-Meier plot shows that the abundance of iCAF predicts poor prognosis of GC using two public bulk RNA sequencing dataset (left, TCGA; right, ACRG). The abundance of iCAF was used to group samples into high and low groups based on 33th and 67th percentile. The *P* value of two-sided log-rank test is shown. ACRG: Asian Cancer Research Group.

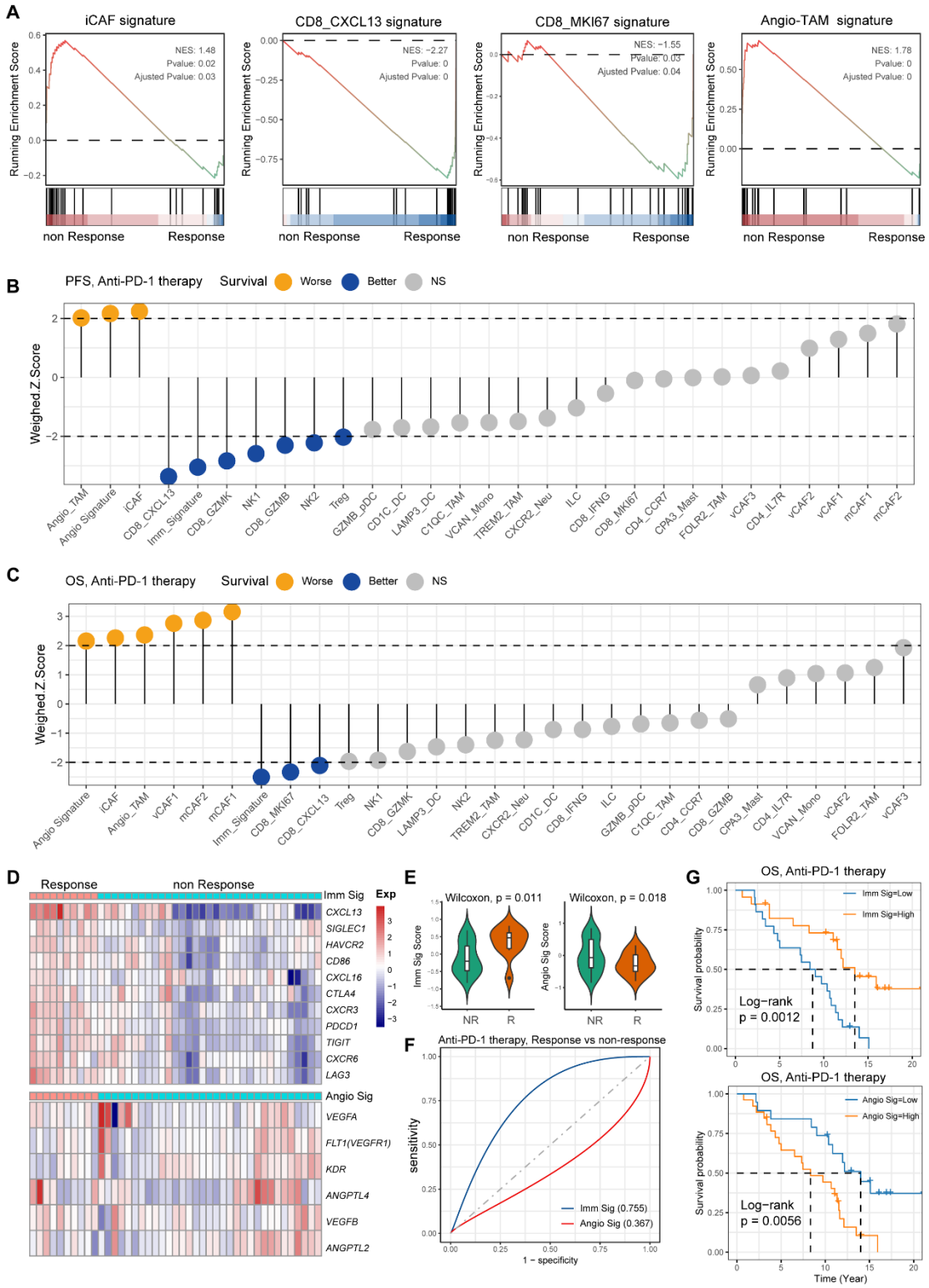

Fig. 7 Single cell TME composition associated with GC immunotherapy outcome. (A) GSEA plot showing the enrichment of iCAF, CD8_MKI67, Angio-TAM, and CD8_CXCL13 in anti-PD1 responsive or non-responsive GC. NES, normalized enrichment score. (B–C) Bar chart showing the cell subtypes relative abundance, the immune signature, angiogenesis signature derived from scRNA-seq predicted GC immunotherapy outcome,

679 progression-free survival (B), and overall survival (C). (D) Heatmap showing the expression of immune and
680 angiogenesis signature derived from scRNA-seq in immunotherapy responsive and non-responsive GC. (E) Violin
681 plot showing the expression of immune signature and angiogenesis signature in immunotherapy responsive and
682 non-responsive GC. The *P* value of Wilcoxon test is shown. (F) A model for evaluating the GC immunotherapy
683 sensitivity and specificity using the immune signature and angiogenesis signature derived from scRNA-seq. (G)
684 The Kaplan-Meier plot showing the immune signature and angiogenesis signature could efficiently predict
685 prognosis of GC anti-PD-1 therapy. The *P* value of two-sided log-rank test is shown.

686 **Table 1: Patient characteristics of each sample in GC scRNA-seq**

Sample	Stage	Age	Sex	Histopathological diagnosis	Site of origin	Lauren's classification	*H. pylori* serum antibody	*H. pylori* DNA	*H. pylori* cagA	*H. pylori* on H&E slide
exHpGC1	III	62	F	Moderately differentiated adenocarcinoma	Gastric antrum and corpus	Intestinal	+	-	-	-
exHpGC2	III	61	M	Moderately differentiated adenocarcinoma	Gastric antrum	Mixed	+	-	-	-
exHpGC3	I	75	M	Poorly differentiated adenocarcinoma	Gastric antrum	Diffuse	+	-	-	-
exHpGC4	II	67	F	Signet ring cell carcinoma	Gastric body	Diffuse	+	-	-	-
exHpGC5	III	64	M	Moderately poorly differentiated adenocarcinoma	Cardia	Intestinal	+	-	-	-
exHpGC6	I	65	M	Moderately differentiated adenocarcinoma	Gastric antrum	Intestinal	+	-	-	-
HpGC1	II	73	M	Moderately poorly differentiated adenocarcinoma	Stomach angle	Intestinal	+	+	-	+
HpGC2	IV	55	M	Poorly differentiated adenocarcinoma	Gastric antrum and corpus	Diffuse	+	+	-	+
HpGC3	I	49	F	Moderately-well differentiated adenocarcinoma	Gastric antrum and gastric angle	Intestinal	+	+	-	+
HpGC4	I	47	M	Poorly differentiated adenocarcinoma, mostly signet ring cell carcinoma	Gastric antrum	Diffuse	+	+	-	+
HpGC5	II	67	F	Signet ring cell carcinoma	Gastric antrum	Diffuse	+	+	-	+
HpGC6	I	58	M	Moderately poorly differentiated adenocarcinoma	Greater curvature	Mixed	+	+	+	+
HpGC7	III	67	F	Moderately poorly differentiated adenocarcinoma	Angular incisure	Intestinal	+	+	N/A	+
HpGC8	III	74	M	Moderately poorly differentiated adenocarcinoma	Greater curvature	Intestinal	+	+	N/A	+
HpGC9	II	62	M	Poorly differentiated adenocarcinoma, partial signet ring cell carcinoma	Angular incisure	Mixed	+	+	N/A	+
nonHpGC1	I	54	F	Poorly differentiated adenocarcinoma	Cardia	Diffuse	-	-	N/A	-
nonHpGC2	III	65	M	Moderately differentiated adenocarcinoma	Cardia	Intestinal	-	-	N/A	-
nonHpGC3	III	56	M	Moderately differentiated adenocarcinoma	Cardia	Intestinal	-	-	N/A	-
nonHpGC4	III	72	M	Moderately poorly differentiated adenocarcinoma	Angular incisure	Intestinal	-	-	N/A	-
nonHpGC5	I	56	M	Poorly differentiated adenocarcinoma	Antrum	Mixed	-	-	N/A	-
nonHpGC6	II	63	M	Poorly differentiated adenocarcinoma	Angular incisure	Mixed	-	-	N/A	-

HC1	N/A	38	M	Normal	Greater curvature	N/A	-	-	N/A	-
HC2	N/A	43	F	Normal	Greater curvature	N/A	-	-	N/A	-
HC3	N/A	62	F	Chronic gastritis	Gastric body	N/A	-	-	-	-
HC4	N/A	61	F	Normal	Gastric antrum	N/A	-	-	-	-
HC5	N/A	25	M	Normal	Gastric antrum	N/A	-	-	-	-
HC6	N/A	32	F	Normal	Gastric antrum	N/A	-	-	-	-

696

697 **Reference**

698 1. Y. Oya, Y. Hayakawa, K. Koike, Tumor microenvironment in gastric cancers. *Cancer*
699 *Sci* **111**, 2696-2707 (2020).

700 2. N. Uemura, S. Okamoto, S. Yamamoto, N. Matsumura, S. Yamaguchi, M. Yamakido,
701 K. Taniyama, N. Sasaki, R. J. Schlemper, Helicobacter pylori infection and the
702 development of gastric cancer. *The New England journal of medicine* **345**, 784-789
703 (2001).

704 3. P. I. Hsu, K. H. Lai, P. N. Hsu, G. H. Lo, H. C. Yu, W. C. Chen, F. W. Tsay, H. C. Lin,
705 H. H. Tseng, L. P. Ger, H. C. Chen, Helicobacter pylori infection and the risk of gastric
706 malignancy. *The American journal of gastroenterology* **102**, 725-730 (2007).

707 4. M. Plummer, S. Franceschi, J. Vignat, D. Forman, C. de Martel, Global burden of
708 gastric cancer attributable to Helicobacter pylori. *International journal of cancer* **136**,
709 487-490 (2015).

710 5. P. Oster, L. Vaillant, E. Riva, B. McMillan, C. Begka, C. Truntzer, C. Richard, M. M.
711 Leblond, M. Messaoudene, E. Machremi, E. Limagne, F. Ghiringhelli, B. Routy, G.
712 Verdeil, D. Velin, Helicobacter pylori infection has a detrimental impact on the efficacy
713 of cancer immunotherapies. *Gut* **71**, 457-466 (2022).

714 6. M. Hatakeyama, The role of Helicobacter pylori CagA in gastric carcinogenesis. *Int J*
715 *Hematol* **84**, 301-308 (2006).

716 7. H. W. Kwak, I. J. Choi, S. J. Cho, J. Y. Lee, C. G. Kim, M. C. Kook, K. W. Ryu, Y. W.
717 Kim, Characteristics of gastric cancer according to Helicobacter pylori infection status.

718 *J Gastroenterol Hepatol* **29**, 1671-1677 (2014).

719 8. S. Y. Son, C. H. Lee, S. Y. Lee, Different Metabolites of the Gastric Mucosa between
720 Patients with Current Helicobacter pylori Infection, Past Infection, and No Infection
721 History. *Biomedicines* **10**, (2022).

722 9. J. A. Thompson, New NCCN Guidelines: Recognition and Management of
723 Immunotherapy-Related Toxicity. *J Natl Compr Canc Netw* **16**, 594-596 (2018).

724 10. M. S. Carlino, J. Larkin, G. V. Long, Immune checkpoint inhibitors in melanoma.
725 *Lancet* **398**, 1002-1014 (2021).

726 11. S. Bagchi, R. Yuan, E. G. Engleman, Immune Checkpoint Inhibitors for the Treatment
727 of Cancer: Clinical Impact and Mechanisms of Response and Resistance. *Annual*
728 *review of pathology* **16**, 223-249 (2021).

729 12. D. B. Doroshow, S. Bhalla, M. B. Beasley, L. M. Sholl, K. M. Kerr, S. Gnjatic, Wistuba,
730 II, D. L. Rimm, M. S. Tsao, F. R. Hirsch, PD-L1 as a biomarker of response to
731 immune-checkpoint inhibitors. *Nature reviews. Clinical oncology* **18**, 345-362 (2021).

732 13. Y. Shi, H. Zheng, M. Wang, S. Ding, Influence of Helicobacter pylori infection on PD-
733 1/PD-L1 blockade therapy needs more attention. *Helicobacter* **27**, e12878 (2022).

734 14. Y. J. Bang, E. Y. Ruiz, E. Van Cutsem, K. W. Lee, L. Wyrwicz, M. Schenker, M.
735 Alsina, M. H. Ryu, H. C. Chung, L. Evesque, S. E. Al-Batran, S. H. Park, M.
736 Lichinitser, N. Boku, M. H. Moehler, J. Hong, H. Xiong, R. Hallwachs, I. Conti, J.
737 Taieb, Phase III, randomised trial of avelumab versus physician's choice of
738 chemotherapy as third-line treatment of patients with advanced gastric or gastro-
739 oesophageal junction cancer: primary analysis of JAVELIN Gastric 300. *Annals of*

740 *oncology : official journal of the European Society for Medical Oncology / ESMO* **29**,
741 2052-2060 (2018).
742 15. K. Shitara, M. Özgüroğlu, Y. J. Bang, M. Di Bartolomeo, M. Mandalà, M. H. Ryu, L.
743 Fornaro, T. Olesiński, C. Caglevic, H. C. Chung, K. Muro, E. Goekkurt, W. Mansoor,
744 R. S. McDermott, E. Shacham-Shmueli, X. Chen, C. Mayo, S. P. Kang, A. Ohtsu, C.
745 S. Fuchs, Pembrolizumab versus paclitaxel for previously treated, advanced gastric
746 or gastro-oesophageal junction cancer (KEYNOTE-061): a randomised, open-label,
747 controlled, phase 3 trial. *Lancet (London, England)* **392**, 123-133 (2018).
748 16. K. Shitara, E. Van Cutsem, Y. J. Bang, C. Fuchs, L. Wyrwicz, K. W. Lee, I. Kudaba, M.
749 Garrido, H. C. Chung, J. Lee, H. R. Castro, W. Mansoor, M. I. Braghiroli, N. Karaseva,
750 C. Caglevic, L. Villanueva, E. Goekkurt, H. Satake, P. Enzinger, M. Alsina, A. Benson,
751 J. Chao, A. H. Ko, Z. A. Wainberg, U. Kher, S. Shah, S. P. Kang, J. Tabernero,
752 Efficacy and Safety of Pembrolizumab or Pembrolizumab Plus Chemotherapy vs
753 Chemotherapy Alone for Patients With First-line, Advanced Gastric Cancer: The
754 KEYNOTE-062 Phase 3 Randomized Clinical Trial. *JAMA oncology* **6**, 1571-1580
755 (2020).
756 17. K. Shitara, J. A. Ajani, M. Moehler, M. Garrido, C. Gallardo, L. Shen, K. Yamaguchi, L.
757 Wyrwicz, T. Skoczylas, A. C. Bragagnoli, T. Liu, M. Tehfe, E. Elimova, R. Bruges, T.
758 Zander, S. de Azevedo, R. Kowalyszyn, R. Pazo-Cid, M. Schenker, J. M. Cleary, P.
759 Yanez, K. Feeney, M. V. Karamouzis, V. Poulart, M. Lei, H. Xiao, K. Kondo, M. Li, Y.
760 Y. Janjigian, Nivolumab plus chemotherapy or ipilimumab in gastro-oesophageal
761 cancer. *Nature* **603**, 942-948 (2022).

762 18. Z. Zhang, Z. Liu, Z. Chen, Comparison of Treatment Efficacy and Survival Outcomes
763 Between Asian and Western Patients With Unresectable Gastric or Gastro-
764 Esophageal Adenocarcinoma: A Systematic Review and Meta-Analysis. *Front Oncol*
765 **12**, 831207 (2022).
766 19. L. Peng, B. D. Qin, K. Xiao, S. Xu, J. S. Yang, Y. S. Zang, J. Stebbing, L. P. Xie, A
767 meta-analysis comparing responses of Asian versus non-Asian cancer patients to
768 PD-1 and PD-L1 inhibitor-based therapy. *Oncoimmunology* **9**, 1781333 (2020).
769 20. S. H. Gohil, J. B. Iorgulescu, D. A. Braun, D. B. Keskin, K. J. Livak, Applying high-
770 dimensional single-cell technologies to the analysis of cancer immunotherapy. *Nature*
771 *reviews. Clinical oncology* **18**, 244-256 (2021).
772 21. S. Z. Wu, A. Swarbrick, Single-cell advances in stromal-leukocyte interactions in
773 cancer. *Immunological reviews*, (2021).
774 22. P. Zhang, M. Yang, Y. Zhang, S. Xiao, X. Lai, A. Tan, S. Du, S. Li, Dissecting the
775 Single-Cell Transcriptome Network Underlying Gastric Premalignant Lesions and
776 Early Gastric Cancer. *Cell Rep* **27**, 1934-1947.e1935 (2019).
777 23. M. Zhang, S. Hu, M. Min, Y. Ni, Z. Lu, X. Sun, J. Wu, B. Liu, X. Ying, Y. Liu,
778 Dissecting transcriptional heterogeneity in primary gastric adenocarcinoma by single
779 cell RNA sequencing. *Gut* **70**, 464-475 (2021).
780 24. R. Wang, M. Dang, K. Harada, G. Han, F. Wang, M. Pool Pizzi, M. Zhao, G.
781 Tatlonghari, S. Zhang, D. Hao, Y. Lu, S. Zhao, B. D. Badgwell, M. Blum Murphy, N.
782 Shanbhag, J. S. Estrella, S. Roy-Chowdhuri, A. A. F. Abdelhakeem, Y. Wang, G.
783 Peng, S. Hanash, G. A. Calin, X. Song, Y. Chu, J. Zhang, M. Li, K. Chen, A. J. Lazar,

784 A. Futreal, S. Song, J. A. Ajani, L. Wang, Single-cell dissection of intratumoral
785 heterogeneity and lineage diversity in metastatic gastric adenocarcinoma. *Nature*
786 *medicine* **27**, 141-151 (2021).
787 25. K. Fu, B. Hui, Q. Wang, C. Lu, W. Shi, Z. Zhang, D. Rong, B. Zhang, Z. Tian, W.
788 Tang, H. Cao, X. Wang, Z. Chen, Single-cell RNA sequencing of immune cells in
789 gastric cancer patients. *Aging* **12**, 2747-2763 (2020).
790 26. A. Sathe, S. M. Grimes, B. T. Lau, J. Chen, C. Suarez, R. J. Huang, G. Poultsides, H.
791 P. Ji, Single-Cell Genomic Characterization Reveals the Cellular Reprogramming of
792 the Gastric Tumor Microenvironment. *Clinical cancer research : an official journal of*
793 *the American Association for Cancer Research* **26**, 2640-2653 (2020).
794 27. R. Kim, M. An, H. Lee, A. Mehta, Y. J. Heo, K. M. Kim, S. Y. Lee, J. Moon, S. T. Kim,
795 B. H. Min, T. J. Kim, S. Y. Rha, W. K. Kang, W. Y. Park, S. J. Klempner, J. Lee, Early
796 Tumor-Immune Microenvironmental Remodeling and Response to First-Line
797 Fluoropyrimidine and Platinum Chemotherapy in Advanced Gastric Cancer. *Cancer*
798 *discovery* **12**, 984-1001 (2022).
799 28. R. Cristescu, J. Lee, M. Nebozhyn, K. M. Kim, J. C. Ting, S. S. Wong, J. Liu, Y. G.
800 Yue, J. Wang, K. Yu, X. S. Ye, I. G. Do, S. Liu, L. Gong, J. Fu, J. G. Jin, M. G. Choi, T.
801 S. Sohn, J. H. Lee, J. M. Bae, S. T. Kim, S. H. Park, I. Sohn, S. H. Jung, P. Tan, R.
802 Chen, J. Hardwick, W. K. Kang, M. Ayers, D. Hongyue, C. Reinhard, A. Loboda, S.
803 Kim, A. Aggarwal, Molecular analysis of gastric cancer identifies subtypes associated
804 with distinct clinical outcomes. *Nature medicine* **21**, 449-456 (2015).
805 29. A. J. Bass, V. Thorsson, I. Shmulevich, S. M. Reynolds, M. Miller, B. Bernard, T.

Hinoue, P. W. Laird, C. Curtis, H. Shen, D. J. Weisenberger, N. Schultz, R. Shen, N. Weinhold, D. P. Kelsen, R. Bowlby, A. Chu, K. Kasaian, A. J. Mungall, A. G. Robertson, P. Sipahimalani, A. Cherniack, G. Getz, Y. Liu, M. S. Noble, C. Pedamallu, C. Sougnez, A. Taylor-Weiner, R. Akbani, J.-S. Lee, W. Liu, G. B. Mills, D. Yang, W. Zhang, A. Pantazi, M. Parfenov, M. Gulley, M. B. Piazuelo, B. G. Schneider, J. Kim, A. Boussioutas, M. Sheth, J. A. Demchok, C. S. Rabkin, J. E. Willis, S. Ng, K. Garman, D. G. Beer, A. Pennathur, B. J. Raphael, H.-T. Wu, R. Odze, H. K. Kim, J. Bowen, K. M. Leraas, T. M. Lichtenberg, S. Weaver, M. McLellan, M. Wiznerowicz, R. Sakai, G. Getz, C. Sougnez, M. S. Lawrence, K. Cibulskis, L. Lichtenstein, S. Fisher, S. B. Gabriel, E. S. Lander, L. Ding, B. Niu, A. Ally, M. Balasundaram, I. Birol, R. Bowlby, D. Brooks, Y. S. N. Butterfield, R. Carlsen, A. Chu, J. Chu, E. Chuah, H.-J. E. Chun, A. Clarke, N. Dhalla, R. Guin, R. A. Holt, S. J. M. Jones, K. Kasaian, D. Lee, H. A. Li, E. Lim, Y. Ma, M. A. Marra, M. Mayo, R. A. Moore, A. J. Mungall, K. L. Mungall, K. Ming Nip, A. G. Robertson, J. E. Schein, P. Sipahimalani, A. Tam, N. Thiessen, R. Beroukhim, S. L. Carter, A. D. Cherniack, J. Cho, K. Cibulskis, D. DiCara, S. Frazer, S. Fisher, S. B. Gabriel, N. Gehlenborg, D. I. Heiman, J. Jung, J. Kim, E. S. Lander, M. S. Lawrence, L. Lichtenstein, P. Lin, M. Meyerson, A. I. Ojesina, C. Sekhar Pedamallu, G. Saksena, S. E. Schumacher, C. Sougnez, P. Stojanov, B. Tabak, A. Taylor-Weiner, D. Voet, M. Rosenberg, T. I. Zack, H. Zhang, L. Zou, A. Protopopov, N. Santoso, M. Parfenov, S. Lee, J. Zhang, H. S. Mahadeshwar, J. Tang, X. Ren, S. Seth, L. Yang, A. W. Xu, X. Song, A. Pantazi, R. Xi, C. A. Bristow, A. Hadjipanayis, J. Seidman, L. Chin, P. J. Park, R. Kucherlapati, R. Akbani, S. Ling, W. Liu, A. Rao, J. N.

828 Weinstein, S.-B. Kim, J.-S. Lee, Y. Lu, G. Mills, P. W. Laird, T. Hinoue, D. J.
829 Weisenberger, M. S. Bootwalla, P. H. Lai, H. Shen, T. Triche Jr, D. J. Van Den Berg,
830 S. B. Baylin, J. G. Herman, G. Getz, L. Chin, Y. Liu, B. A. Murray, M. S. Noble, r. B.
831 Arman Askoy, G. Ciriello, G. Dresdner, J. Gao, B. Gross, A. Jacobsen, W. Lee, R.
832 Ramirez, C. Sander, N. Schultz, Y. Senbabaoglu, R. Sinha, S. Onur Sumer, Y. Sun,
833 N. Weinhold, V. Thorsson, B. Bernard, L. Iype, R. W. Kramer, R. Kreisberg, M. Miller,
834 S. M. Reynolds, H. Rovira, N. Tasman, I. Shmulevich, S. Ng, D. Haussler, J. M.
835 Stuart, R. Akbani, S. Ling, W. Liu, A. Rao, J. N. Weinstein, R. G. W. Verhaak, G. B.
836 Mills, M. D. M. Leiserson, B. J. Raphael, H.-T. Wu, B. S. Taylor, A. D. Black, J.
837 Bowen, J. Ann Carney, J. M. Gastier-Foster, C. Helsel, K. M. Leraas, T. M.
838 Lichtenberg, C. McAllister, N. C. Ramirez, T. R. Tabler, L. Wise, E. Zmuda, R. Penny,
839 D. Crain, J. Gardner, K. Lau, E. Curely, D. Mallery, S. Morris, J. Paulauskis, T.
840 Shelton, C. Shelton, M. Sherman, C. Benz, J.-H. Lee, K. Fedosenko, G. Manikhas, O.
841 Potapova, O. Voronina, D. Belyaev, O. Dolzhansky, W. Kimryn Rathmell, J.
842 Brzezinski, M. Ibbs, K. Korski, N. The Cancer Genome Atlas Research, I. Analysis
843 Working Group: Dana-Farber Cancer, B. Institute for Systems, C. University of
844 Southern, C. Memorial Sloan Kettering Cancer, B. C. C. Agency, E. The, L. B. I.
845 Edythe, M. D. A. C. Center, S. Harvard Medical, C. University of North, U. Vanderbilt,
846 C. Asan Medical, M. University of, I. National Cancer, U. Case Western Reserve, C.
847 University of California at Santa, U. Duke, M. University of, P. University of, U. Brown,
848 Brigham, H. Women's, C. National Cancer, H. Nationwide Children's, U. Washington,
849 C. Greater Poland Cancer, K. U. Leuven, E. Genome Sequencing Center: The, L. B. I.

850 Edythe, L. Washington University in St, B. C. C. A. Genome Characterization Centers,
851 S. B. Harvard Medical, M. D. A. C. C. Women's Hospital, C. University of Southern
852 California Epigenome, U. The Sidney Kimmel Comprehensive Cancer Center at
853 Johns Hopkins, E. Genome Data Analysis Centers: The, L. B. I. Edythe, C. Memorial
854 Sloan-Kettering Cancer, S. C. University of California, F. University of California San,
855 H. Biospecimen Core Resource: The Research Institute at Nationwide Children's, C.
856 International Genomics, A. Tissue Source Sites: Buck Institute for Research on, S.
857 Chonnam National University Medical, D. City Clinical Oncology, Cureline, U. N. C. L.
858 C. C. Center, Comprehensive molecular characterization of gastric adenocarcinoma.
859 *Nature* **513**, 202-209 (2014).
860 30. J. M. Chauvin, H. M. Zarour, TIGIT in cancer immunotherapy. *J Immunother Cancer* **8**,
861 (2020).
862 31. H. Harjunpaa, C. Guillerey, TIGIT as an emerging immune checkpoint. *Clin Exp*
863 *Immunol* **200**, 108-119 (2020).
864 32. Z. Ge, M. P. Peppelenbosch, D. Sprengers, J. Kwekkeboom, TIGIT, the Next Step
865 Towards Successful Combination Immune Checkpoint Therapy in Cancer. *Front*
866 *Immunol* **12**, 699895 (2021).
867 33. C. Lin, H. He, H. Liu, R. Li, Y. Chen, Y. Qi, Q. Jiang, L. Chen, P. Zhang, H. Zhang, H.
868 Li, W. Zhang, Y. Sun, J. Xu, Tumour-associated macrophages-derived CXCL8
869 determines immune evasion through autonomous PD-L1 expression in gastric cancer.
870 *Gut* **68**, 1764-1773 (2019).
871 34. X. Chen, E. Song, Turning foes to friends: targeting cancer-associated fibroblasts.

872 *Nat Rev Drug Discov* **18**, 99-115 (2019).

873 35. T. Nishina, Y. Deguchi, D. Ohshima, W. Takeda, M. Ohtsuka, S. Shichino, S. Ueha, S.
874 Yamazaki, M. Kawauchi, E. Nakamura, C. Nishiyama, Y. Kojima, S. Adachi-Akahane,
875 M. Hasegawa, M. Nakayama, M. Oshima, H. Yagita, K. Shibuya, T. Mikami, N.
876 Inohara, K. Matsushima, N. Tada, H. Nakano, Interleukin-11-expressing fibroblasts
877 have a unique gene signature correlated with poor prognosis of colorectal cancer.
878 *Nature communications* **12**, 2281 (2021).

879 36. M. Zhang, H. Yang, L. Wan, Z. Wang, H. Wang, C. Ge, Y. Liu, Y. Hao, D. Zhang, G.
880 Shi, Y. Gong, Y. Ni, C. Wang, Y. Zhang, J. Xi, S. Wang, L. Shi, L. Zhang, W. Yue, X.
881 Pei, B. Liu, X. Yan, Single-cell transcriptomic architecture and intercellular crosstalk
882 of human intrahepatic cholangiocarcinoma. *Journal of hepatology* **73**, 1118-1130
883 (2020).

884 37. S. T. Kim, R. Cristescu, A. J. Bass, K. M. Kim, J. I. Odegaard, K. Kim, X. Q. Liu, X.
885 Sher, H. Jung, M. Lee, S. Lee, S. H. Park, J. O. Park, Y. S. Park, H. Y. Lim, H. Lee, M.
886 Choi, A. Talasaz, P. S. Kang, J. Cheng, A. Loboda, J. Lee, W. K. Kang,
887 Comprehensive molecular characterization of clinical responses to PD-1 inhibition in
888 metastatic gastric cancer. *Nature medicine* **24**, 1449-1458 (2018).

889 38. X. Hong, B. Cui, M. Wang, Z. Yang, L. Wang, Q. Xu, Systemic Immune-inflammation
890 Index, Based on Platelet Counts and Neutrophil-Lymphocyte Ratio, Is Useful for
891 Predicting Prognosis in Small Cell Lung Cancer. *The Tohoku journal of experimental*
892 *medicine* **236**, 297-304 (2015).

893 39. L. E. Wroblewski, R. M. Peek, Jr., K. T. Wilson, Helicobacter pylori and gastric cancer:

894 factors that modulate disease risk. *Clin Microbiol Rev* **23**, 713-739 (2010).

895 40. H. Chang, N. Kim, J. H. Park, R. H. Nam, Y. J. Choi, S. M. Park, Y. J. Choi, H. Yoon,
896 C. M. Shin, D. H. Lee, Helicobacter pylori Might Induce TGF-β1-Mediated EMT by
897 Means of cagE. *Helicobacter* **20**, 438-448 (2015).

898 41. R. Silva, I. Gullo, F. Carneiro, The PD-1:PD-L1 immune inhibitory checkpoint in
899 Helicobacter pylori infection and gastric cancer: a comprehensive review and future
900 perspectives. *Porto Biomed J* **1**, 4-11 (2016).

901 42. L. Holokai, J. Chakrabarti, T. Broda, J. Chang, J. A. Hawkins, N. Sundaram, L. E.
902 Wroblewski, R. M. Peek, Jr., J. Wang, M. Helmrath, J. M. Wells, Y. Zavros, Increased
903 Programmed Death-Ligand 1 is an Early Epithelial Cell Response to Helicobacter
904 pylori Infection. *PLoS Pathog* **15**, e1007468 (2019).

905 43. B. Shen, A. Qian, W. Lao, W. Li, X. Chen, B. Zhang, H. Wang, F. Yuan, Y. Sun,
906 Relationship between Helicobacter pylori and expression of programmed death-1 and
907 its ligand in gastric intraepithelial neoplasia and early-stage gastric cancer. *Cancer*
908 *Manag Res* **11**, 3909-3919 (2019).

909 44. D. K. Kim, J. Jeong, D. S. Lee, D. Y. Hyeon, G. W. Park, S. Jeon, K. B. Lee, J. Y.
910 Jang, D. Hwang, H. M. Kim, K. Jung, PD-L1-directed PlGF/VEGF blockade
911 synergizes with chemotherapy by targeting CD141(+) cancer-associated fibroblasts in
912 pancreatic cancer. *Nat Commun* **13**, 6292 (2022).

913 45. A. X. Zhu, A. R. Abbas, M. R. de Galarreta, Y. Guan, S. Lu, H. Koeppen, W. Zhang,
914 C.-H. Hsu, A. R. He, B.-Y. Ryoo, T. Yau, A. O. Kaseb, A. M. Burgoyne, F. Dayyani, J.
915 Spahn, W. Verret, R. S. Finn, H. C. Toh, A. Lujambio, Y. Wang, Molecular correlates

916 of clinical response and resistance to atezolizumab in combination with bevacizumab
917 in advanced hepatocellular carcinoma. *Nature medicine*, (2022).
918 46. D. Fukumura, J. Kloepper, Z. Amoozgar, D. G. Duda, R. K. Jain, Enhancing cancer
919 immunotherapy using antiangiogenics: opportunities and challenges. *Nature reviews.*
920 *Clinical oncology* **15**, 325-340 (2018).
921 47. P. S. Hegde, J. J. Wallin, C. Mancao, Predictive markers of anti-VEGF and emerging
922 role of angiogenesis inhibitors as immunotherapeutics. *Seminars in cancer biology* **52**,
923 117-124 (2018).
924 48. S. Ragusa, B. Prat-Luri, A. González-Loyola, S. Nassiri, M. L. Squadrito, A. Guichard,
925 S. Cavin, N. Gjorevski, D. Barras, G. Marra, M. P. Lutolf, J. Perentes, E. Corse, R.
926 Bianchi, L. Wetterwald, J. Kim, G. Oliver, M. Delorenzi, M. De Palma, T. V. Petrova,
927 Antiangiogenic immunotherapy suppresses desmoplastic and chemoresistant
928 intestinal tumors in mice. *The Journal of clinical investigation* **130**, 1199-1216 (2020).
929 49. T. Stuart, A. Butler, P. Hoffman, C. Hafemeister, E. Papalexi, W. M. Mauck, Y. Hao,
930 M. Stoeckius, P. Smibert, R. Satija, Comprehensive Integration of Single-Cell Data.
931 *Cell* **177**, 1888-1902.e1821 (2019).
932 50. C. S. McGinnis, L. M. Murrow, Z. J. Gartner, DoubletFinder: Doublet Detection in
933 Single-Cell RNA Sequencing Data Using Artificial Nearest Neighbors. *Cell Systems* **8**,
934 329-337.e324 (2019).
935 51. I. Tirosh, A. S. Venteicher, C. Hebert, L. E. Escalante, A. P. Patel, K. Yizhak, J. M.
936 Fisher, C. Rodman, C. Mount, M. G. Filbin, C. Neftel, N. Desai, J. Nyman, B. Izar, C.
937 C. Luo, J. M. Francis, A. A. Patel, M. L. Onozato, N. Riggi, K. J. Livak, D. Gennert, R.

938 Satija, B. V. Nahed, W. T. Curry, R. L. Martuza, R. Mylvaganam, A. J. Iafrate, M. P.
939 Frosch, T. R. Golub, M. N. Rivera, G. Getz, O. Rozenblatt-Rosen, D. P. Cahill, M.
940 Monje, B. E. Bernstein, D. N. Louis, A. Regev, M. L. Suvà, Single-cell RNA-seq
941 supports a developmental hierarchy in human oligodendroglioma. *Nature* **539**, 309-
942 313 (2016).
943 52. S. Hänzelmann, R. Castelo, J. Guinney, GSVA: gene set variation analysis for
944 microarray and RNA-Seq data. *BMC bioinformatics* **14**, 7 (2013).
945 53. S. Cheng, Z. Li, R. Gao, B. Xing, Y. Gao, Y. Yang, S. Qin, L. Zhang, H. Ouyang, P.
946 Du, L. Jiang, B. Zhang, Y. Yang, X. Wang, X. Ren, J.-X. Bei, X. Hu, Z. Bu, J. Ji, Z.
947 Zhang, A pan-cancer single-cell transcriptional atlas of tumor infiltrating myeloid cells.
948 *Cell* **184**, 792-809.e723 (2021).
949 54. C. Trapnell, D. Cacchiarelli, J. Grimsby, P. Pokharel, S. Li, M. Morse, N. J. Lennon, K.
950 J. Livak, T. S. Mikkelsen, J. L. Rinn, The dynamics and regulators of cell fate
951 decisions are revealed by pseudotemporal ordering of single cells. *Nature*
952 *biotechnology* **32**, 381-386 (2014).
953 55. S. Jin, C. F. Guerrero-Juarez, L. Zhang, I. Chang, R. Ramos, C. H. Kuan, P. Myung,
954 M. V. Plikus, Q. Nie, Inference and analysis of cell-cell communication using CellChat.
955 *Nature communications* **12**, 1088 (2021).
956
957